

1 **Miocene–Pleistocene deformation of the Saddle Mountains: implications for seismic hazard**
2 **in central Washington, USA**

3 Lydia Staisch^{1,2}, Harvey Kelsey³, Brian Sherrod², Andreas Möller⁴, James Paces⁵, Richard
4 Blakely¹, Richard Styron^{6,7}

5 ¹ *U.S. Geological Survey, Geology, Minerals, Energy and Geophysics Science Center, Menlo Park,*
6 *CA 94025*

7 ² *U.S. Geological Survey, Earthquake Science Center, University of Washington, Seattle, WA*
8 *98195*

9 ³ *Department of Geology, Humboldt State University, Arcata, CA 95521*

10 ⁴ *Department of Geology, The University of Kansas, Lawrence, KS 66045*

11 ⁵ *U.S. Geological Survey, Geoscience and Environmental Change Science Center, Denver, CO*
12 *80225*

13 ⁶ *Earth Analysis, Seattle, WA 98105*

14 ⁷ *Global Earthquake Model Foundation, Pavia, Italy*

15

16 **ABSTRACT**

17 The Yakima fold province, located in the backarc of the Cascadia Subduction Zone, is a
18 region of active strain accumulation and deformation distributed across a series of fault-cored
19 folds. The geodetic network in central Washington has been used to interpret large-scale N-S
20 shortening and westward-increasing strain, however geodetic data are unable to resolve shortening
21 rates across individual structures in this low-strain-rate environment. Resolving fault geometries,
22 slip rates, and timing of faulting in the Yakima fold province are critically important to seismic
23 hazard assessment for nearby infrastructure and population centers.

24 The Saddle Mountains anticline (SMA) is one of the most prominent Yakima folds. It is
25 unique within the Yakima fold province in that the syntectonic strata of the Ringold Formation are
26 preserved and provide a record of deformation and drainage reorganization. Here we present new
27 stratigraphic columns, U-Pb zircon tephra ages, U-series caliche ages, and geophysical modeling
28 that constrain two line-balanced and retrodeformed cross sections. These new constraints indicate
29 that the SMA has accommodated 1.0–1.3 km of N-S shortening since 10 Ma, that shortening
30 increases westward along the anticline, and that the average slip rate has increased 6-fold since 6.8
31 Ma. Provenance analysis suggests that the source terrane for the Ringold Formation is similar to
32 that of the modern Snake River Plain. Using new slip rates and structural constraints, we calculate
33 the strain accumulation time, interpretable as a recurrence interval, for earthquakes on the Saddle
34 Mountains fault (SMF) and find that large magnitude earthquakes could rupture along the SMF
35 every 2–11 kyr.

36

37 **INTRODUCTION**

38 The U.S. Pacific Northwest is a region of considerable seismic hazard, largely owing to the
39 subduction of the Juan de Fuca, Gorda, and Explorer plates beneath North America and clockwise
40 rotation of upper crustal blocks (Fig. 1). Geodetic surveys show that modern strain accumulation
41 extends far inboard of the Cascadia Subduction Zone (McCaffrey et al., 2007; 2013; 2016).
42 Consequently, seismic hazards are not only concentrated near the plate boundary, but also in the
43 backarc.

44 The Yakima fold province, located in central Washington State, is a region of active strain
45 accumulation and distributed deformation across a series of roughly east-west trending fault-cored
46 anticlinal ridges (Fig. 1). The region undergoes ~N-S shortening at 2 mm yr^{-1} due to convergence

47 between the clockwise-rotating Oregon Block to the south and the stable North American Plate to
48 the northeast (Wells et al., 1998; McCaffrey et al., 2000; 2013; 2016). Paleoseismic studies
49 highlight past earthquake occurrence along several Yakima folds (Campbell and Bentley, 1981;
50 West et al., 1996; Blakely et al., 2011). However, fault geometries, slip rates, and the general
51 deformation history of the Yakima folds remain debated and are of critical importance to
52 earthquake hazard assessment for nearby infrastructure, such as the Hanford Site, a large nuclear
53 waste facility, and major dams along the Columbia and Yakima rivers (Fig. 1; Geomatrix
54 Consultants, 1996; Benjamin and Associates et al., 2012).

55 Seismicity, geodetic data, and gravity anomalies within the Yakima fold province share
56 several patterns that may delineate important geologic features and boundaries. Within the region,
57 earthquake epicenters tend to cluster near the Yakima Canyon and near the Saddle Mountains (Fig.
58 1). The Hog Ranch-Naneum anticline (Tabor et al., 1982) is located between these two
59 seismically-active regions and has been identified as a potentially important boundary between two
60 domains of strain within the Yakima fold province by high-resolution geodetic work (McCaffrey et
61 al., 2016). McCaffrey et al. (2016) also identify another boundary located immediately to the east
62 of the Saddle Mountains (Fig. 1). These proposed strain boundaries correspond well with steep
63 gradients in isostatic residual gravity anomaly data and are thus likely long-lived geologic features
64 (Saltus, 1993; Blakely et al., 2011; Lamb et al., 2015). While geodetic data illuminate large-scale
65 trends within central Washington, the overall strain rate is low and noise within geodetic data
66 obscures the signal of active deformation along individual fault-cored folds. The geologic record,
67 on the other hand, encompasses enough time to clarify spatial and temporal variance in strain rate.

68 The Saddle Mountains anticline (SMA) is the most prominent Yakima fold east of the
69 Columbia River and is bracketed by the aforementioned boundaries in gravity and geodetic data

70 (Fig. 1). Its topographic prominence in the landscape and proximity to infrastructure makes it an
71 ideal target for geologic investigation and hazard assessment. The majority of the Yakima fold
72 province is composed of Miocene Columbia River Basalt Group (CRBG), much of which has been
73 stripped of less-consolidated suprabasaltic strata by catastrophic Pleistocene flooding. However,
74 the SMA is unique among the Yakima folds in that post-CRBG Ringold Formation (Packer and
75 Johnson, 1979; Repenning, 1987; Morgan and Morgan, 1995) is preserved in the hanging wall and
76 footwall of the exposed Saddle Mountains fault (SMF; Reidel, 1988). The preservation of these
77 terrestrial strata allows for expansion of the SMA deformation history into post-mid Miocene time.

78 In this work, we examine the Ringold Formation and the magnitude of deformation of the
79 Saddle Mountains anticline to reconstruct the chronology of deformation in central Washington.
80 To establish the sedimentological response to deformation along the anticline, we measure the
81 stratigraphy in the hanging wall and footwall of the SMF, date interbedded tephra using U-Pb
82 zircon geochronology, date variably deformed petrocalcic horizons using U-series geochronology,
83 and determine the source of strata using U-Pb detrital zircon provenance analysis. We evaluate
84 spatial and temporal changes in the deformation rate along the SMA by measuring the offset along
85 variably deformed marker beds. In addition, we construct two new balanced cross sections, further
86 constrained by modeling of high-resolution magnetic anomaly data, to document the magnitude of
87 shortening and along-strike structural variability. Finally, we use new constraints on the structure
88 and deformation rates of the SMA to assess the seismic hazards posed to central Washington.

89

90 **GEOLOGIC BACKGROUND**

91 The Saddle Mountains are a prominent structural feature of the Yakima Fold Province and
92 form the northern boundary of the Pasco Basin in central Washington State. The Saddle Mountains

93 are ~115 km long, spanning from the eastern edge of Kittitas Valley to just south of Othello, WA
94 (Fig. 1). The westward continuation of the Saddle Mountains, west of the Hog Ranch-Naneum
95 anticline, is called the Boylston Mountains, which gradually bend to a northwest-southeast trend
96 (Fig. 1).

97 **Stratigraphy**

98 The Columbia River Basalt Group (CRBG) blanketed eastern Washington and Oregon in the
99 Miocene (Reidel et al., 1989a, 1989b; 1994; 2013), thus the modern topography of the Yakima fold
100 province has been generated since mid-Miocene time (Reidel, 1984; Watters, 1989). While the
101 landscape of eastern and central Washington is largely mantled in Miocene flood basalts,
102 exploratory oil and gas drilling has locally revealed the underlying stratigraphy. In the Saddle
103 Mountains, boreholes BN 1-9 and AF 1-6 (Figs. 1 and 2) (Czajkowski et al., 2012) reached depths
104 >5.3 and >4.3 km, respectively, and penetrated through the CRBG and into the underlying Eocene
105 and Oligocene strata (Figs. 3 and A1). The 400–700 m of strata immediately beneath the CRBG
106 found in borehole logs have been assigned to the Ellensburg Formation (Czajkowski et al., 2012),
107 which is typically a name given to undifferentiated clastic and volcanoclastic strata intercalated
108 with and overlying the CRBG (Bentley, 1977; Smith et al., 1988; Tolan et al., 2009; Cheney,
109 2014). Because of their stratigraphic position below the CRBG, the units identified as Ellensburg
110 formation in boreholes BN 1-9 and AF 1-6 are more likely either the andesitic to basaltic
111 Oligocene Fifes Peak or the clastic and tuffaceous Ohanapecosh Formations (Fig. 3; Fiske, 1963;
112 Smith et al., 1988; Tabor et al., 2000; Cheney, 2014; Jutzeler et al., 2014). Logs from boreholes
113 BN 1-9 and AF 1-6 indicate that basalt continues below the CRBG strata (Wilson et al., 2008;
114 Czajkowski et al., 2012), suggesting that the Oligocene strata are more likely the Fifes Peak
115 Formation at these locations (Fig. A1). Beneath the Oligocene strata, boreholes penetrate into 240–

116 400 m of mid Eocene Wenatchee Formation and 520–1420 m of mid-late Eocene Roslyn
117 Formation, both of which are typically fluvial and lacustrine in lithology (Figs. 3 and A1; Tabor et
118 al., 1984; Miller et al., 2009; Gilmour, 2012; Cheney, 2014). Neither borehole AF 1-6 nor BN 1-9
119 penetrates into basement rock. North of the Saddle Mountains, boreholes Brown 7-24 and Quincy
120 No. 1 penetrate into underlying Oligocene and Eocene strata and the latter terminates in basement
121 rock, thus limiting the pre-Miocene stratigraphic thickness locally to 1690 m (Fig. A1). Overall,
122 the boreholes drilled near the Saddle Mountains show a northward thinning of pre-Miocene strata.

123 The oldest rock unit exposed on the Saddle Mountains is the Grande Ronde Basalt, part of
124 the Columbia River Basalt Group, emplaced 16.0–15.6 Ma (Fig. 3; Swanson et al., 1979; Camp,
125 1981; Barry et al., 2013). The Grande Ronde Basalt is divided into four major sections based on
126 their geomagnetic polarity. From oldest to youngest, these sections are R₁, N₁, R₂, N₂ and each
127 section is further divided into individual flow groups based on geochemistry (Reidel, 1983; Reidel
128 et al., 2013). The majority of Grande Ronde Basalt exposures in the Saddle Mountains are of the
129 upper, normal-polarity N₂ flows, which include the Sentinel Bluffs Member (Tsb; Fig. 2).
130 However, exposures of the underlying, reverse-polarity R₂ flows are observed near Sentinel Gap,
131 including the Schwana geochemical group (Ts; Fig. 2; Coe et al., 1978; Reidel, 1984).

132 The Wanapum Basalt stratigraphically overlies the Grande Ronde Basalt (Fig. 3). In the
133 Saddle Mountains, exposures of this unit are limited to the Frenchman Springs (Tf), Roza (Tr), and
134 Priest Rapids Members (Tpr), which were emplaced ca. 15.5–14.5 Ma (Swanson et al., 1979;
135 Camp, 1981; Reidel and Fecht, 1981). Within the Pasco Basin, south of the Saddle Mountains,
136 other Wanapum Basalt flows have been mapped, but are less laterally extensive and did not reach
137 the Saddle Mountains (Reidel and Fecht, 1981).

138 The Saddle Mountains Basalt overlies the Wanapum Basalt (Fig. 3). The Huntzinger Flow
139 (Th; 13.3–13.0 Ma), Pomona (Tp; 12.0–10.9 Ma), Elephant Mountain (Tem; 10.5–10.0 Ma), and
140 Ice Harbor (8.8–8.5 Ma) Members of the Saddle Mountains Basalt are exposed in the Saddle
141 Mountains and were erupted between ~14 and 8.5 Ma (Swanson et al., 1979; Camp, 1981; Reidel
142 and Fecht, 1981; 1987; Reidel et al., 2013). The Ice Harbor Member exposures are very limited on
143 Saddle Mountain (Reidel, 1988), and thus the majority of the CRBG strata along the Saddle
144 Mountains were erupted prior to 10 Ma.

145 The majority of suprabasaltic strata on the Saddle Mountains are exposed on Smyrna
146 Bench, in the footwall of the Saddle Mountains fault (Tru; Figs. 2 and 3). However, limited
147 outcrops of strata have been identified on the hanging wall of the SMF (Fig. 2; Reidel, 1988). The
148 age of suprabasaltic strata in the footwall and hanging wall of the SMF was not geochronologically
149 or biostratigraphically constrained prior to this work. Existing mapping shows that these units
150 overlie the 10.5–10.0 Ma Elephant Mountain Member and have been interpreted to be part of the
151 Miocene–Pliocene Ringold Formation (Packer and Johnson, 1979; Repenning, 1987; Reidel, 1988;
152 Morgan and Morgan, 1995). Paleomagnetic studies conducted on the Taunton and White Bluffs
153 exposures concluded that deposition of the upper Ringold Formation occurred during the Gilbert
154 Epoch (Packer and Johnson, 1979) identified by Gradstein et al. (2012) as (6.033–3.596 Ma).
155 Mammalian and fish fossil evidence suggests that deposition continued into the Kaena subchron of
156 the Gauss Epoch (Morgan and Morgan, 1995; Repenning, 1987), from 3.032–3.116 Ma (Gradstein
157 et al., 2012). However, the outcrops on the Saddle Mountains differ from typical Ringold
158 Formation strata, which is best exposed at the White Bluffs along the Columbia River and near the
159 town of Taunton, WA, southeast of the Saddle Mountains, respectively (Fig. 1). Specifically,
160 outcrops along the Saddle Mountains include a much greater volume of conglomeratic strata,

161 compared to the strata dominated by lacustrine and paleosols facies along the White Bluffs and
162 near Taunton. Furthermore, lithofacies and stratigraphic thicknesses of the Ringold Formation vary
163 significantly and may record local geologic events, such as deformation along a nearby structure,
164 as well as large-scale events, such as drainage reorganization (Lindsey and Gaylord, 1990).

165 **Structure**

166 The dominant structure of the Saddle Mountains is the east-west trending, north-vergent,
167 asymmetrical Saddle Mountains anticline (SMA), which is cored by the south-dipping Saddle
168 Mountains reverse fault (SMF). The Crest anticline and the Smyrna monocline are smaller
169 structures on the Saddle Mountains that similarly trend east-west (Figs. 1 and 2). Other structural
170 features of the Saddle Mountains include the less apparent northwest-southeast trending Smyrna
171 fault and a small but well exposed anticline located near the western extent of the Crest anticline
172 (Fig. 2).

173 During the latest Pleistocene, several cataclysmic outburst floods from glacial Lake
174 Missoula flowed through the Crab Creek scablands-channel system, along the northern margin of
175 the Saddle Mountains, and incised through the Saddle Mountains at what is now Sentinel Gap
176 (Smith et al., 1993). The floods through the Crab Creek channel likely eroded the western extent of
177 the Smyrna Bench (Fig. 2), and bared a cross-sectional exposure of the SMF (Fig. 4). At the
178 exposure of the SMF and along Smyrna Bench, the SMF places Miocene CRBG in the hanging
179 wall over the Smyrna Bench, which is composed of CRBG strata and suprabasaltic strata. Further
180 west, the SMF footwall is not well exposed due to glacial outburst flood erosion and concealment
181 beneath alluvial fans. East of the Smyrna Bench, the SMF does not appear to be exposed, as the
182 Elephant Mountain Member is folded at the surface, but not faulted (Fig. 2; Reidel, 1988).

183 Based on seismic reflection data collected near Sentinel Gap, Casale and Pratt (2015) argue
184 for two possibilities for SMF geometry at depth: (1) a low-angle fault geometry, which would
185 require a two stacked décollement at depth, or (2) a high-angle fault geometry, which would
186 require the SMF fault trace to be several hundreds of meters north of its current mapped location.
187 We note that alluvium obscures the fault location along the seismic reflection transect (Fig. 2). The
188 two proposed models vary not only in fault geometry at depth, but also in the potential earthquake
189 hazards posed to central Washington. Casale and Pratt (2015) argue that the high-angle fault
190 geometry model increases the area over which a single earthquake along the Saddle Mountains
191 fault could rupture, and thus increases the maximum magnitude of potential seismic events to
192 $M > 7.5$.

193 Structural and geophysical observations suggest that there may be a component of lateral
194 shear accommodated near the Saddle Mountains. High-resolution aeromagnetic data show strong
195 magnetic anomalies along the Smyrna anticline, which may relate to ponding of basalts along the
196 eastern edge of the anticline (Reidel, 1984; Blakely et al., 2011). The Smyrna fault, which is
197 parallel to and west of the Smyrna anticline, accommodates minor right lateral offset based on
198 displacement of CRBG flows (Reidel, 1984). Similarly, Reidel (1984) suggests that the SMA is
199 offset 2.7 km on either side of the Sentinel Gap (Fig. 2). Alternatively, offset may be
200 accommodated by bending of the anticlinal crest or by lateral or oblique ramps along the SMF.
201 Evidence for either model is obscured by erosion along the Columbia River.

202 **Previous work on the timing of deformation**

203 While deformation along the Saddle Mountains is mainly preserved in the CRBG, several
204 studies suggest that deformation initiated prior to the Miocene and continues today (Malone et al.,
205 1975; West et al., 1996; Casale and Pratt, 2015). Seismic reflection data across the Saddle

206 Mountains reveal a steepening of bedding orientations below ~4 km depth (Pratt et al., 2012;
207 Casale and Pratt, 2015). Results from borehole BN 1-9, drilled at the hinge of the Crest anticline
208 (Czajkowski et al., 2012), indicate the change in bedding orientations may occur between the
209 Eocene Roslyn Formation (48–45 Ma; Tabor et al., 1984; Miller et al., 2009; Cheney, 2014) and
210 the overlying mid Eocene Wenatchee Formation (>44.5–34(?) Ma; Tabor et al., 1984; Gilmour,
211 2012; Cheney, 2014). This may suggest that displacement was accommodated along the SMA
212 and/or SMF between mid-late Eocene and early Oligocene time. Seismic reflection and borehole
213 data do not penetrate beneath the Roslyn formation, and so we have little insight as to whether the
214 initiation of deformation along the SMA and SMF preceded or postdated Eocene deposition.

215 Variations in basalt flow thickness have been used to constrain the timing of deformation
216 (Reidel, 1984). Thinning of the Grande Ronde Basalt towards the east-west trending anticlinal
217 ridges near Sentinel Gap and near the Smyrna anticlinal ridge may suggest that deformation on the
218 SMF-SMA system was active during deposition from 16.0–15.6 Ma (Reidel, 1984). Similarly, the
219 Huntzinger and Pomona flows (13.3–10.9 Ma) thin northward and do not extend north of the
220 SMA, which may also relate to syndepositional deformation (Reidel, 1984). However, the more
221 recent borehole data show continued thinning of CRBG units north of the SMA (Fig. A1),
222 suggesting that this variation in flow thickness could alternatively be controlled by subsidence of
223 the Pasco Basin (Reidel et al. 1989a; 2013), rather than being controlled by local anticlinal growth.
224 We note that these two hypotheses are not mutually exclusive.

225 Folding of the Ringold Formation in the hanging wall of the SMF suggests that north-south
226 shortening across the SMF likely continued into late Miocene–Pliocene time (Reidel, 1984). A
227 paleoseismic study conducted along the Smyrna Bench provides evidence for Holocene
228 deformation along the SMF (West et al., 1996). Additionally, composite stress tensors from

229 microearthquakes near the Saddle Mountains are compatible with north-south shortening and thus
230 may indicate modern activity along the SMF and associated anticlines (Malone et al., 1975).

231

232 **STRATIGRAPHY**

233 In this work, we present six new stratigraphic sections measured in the suprabasaltic
234 Ringold Formation near the Saddle Mountains. Four stratigraphic sections were measured in the
235 hanging wall of the Saddle Mountains fault and two sections were measured in the footwall (Figs.
236 2 and 5). Sections were measured at decimeter scale and the base of all sections began at the top of
237 the 10–10.5 Ma Elephant Mountain Member of the Saddle Mountains Basalt (Reidel, 1984). Strata
238 measured in the hanging wall of the Saddle Mountains fault were typically very well exposed (Fig.
239 6A). The quality of exposure of footwall strata was more variable, ranging from excellent to
240 moderate.

241 We identified eleven distinct lithofacies in the hanging wall and footwall strata of the
242 Saddle Mountains (Table 1). Facies V1 and V2 represent volcanic units interbedded within the
243 Ringold Formation. Given its stratigraphic position above the Elephant Mountain Member, the
244 weathered basalt (facies V1) is likely one of the smaller Saddle Mountain Basalt flows erupted
245 during the waning stages of CRBG volcanism (Reidel, 1984; Reidel et al., 2013). Facies V2 is
246 interpreted as air fall tuff erupted during sediment accumulation along the SMA. Facies C1-C4 are
247 dominantly conglomeratic or associated with conglomerate strata (Table 1). Facies L1 and L2 are
248 associated with lacustrine strata, which are only present in the upper footwall sections. These facies
249 are similar to those documented in most other studies of the Ringold Formation (Packer and
250 Johnson, 1979; Repenning, 1987; Lindsey and Gaylord, 1990; Morgan and Morgan, 1995;
251 Lindsey, 1996). Facies A1 represents aeolian loess and is found throughout the measured strata.

252 Facies P1 and P2, found throughout the measured strata, are pedogenic horizons that represent soil
253 formation during depositional hiatuses. Soil structure varies from weak blocky to well-developed
254 prismatic, suggesting variable durations of land surface stability. Vertical burrows and root casts
255 are common in paleosols. Petrocalcite horizons (i.e. caliche) developed within layers of open-
256 framework conglomeratic, aeolian, and lacustrine strata (Figs. 6B, 6C, 6E, and 6F) and are
257 typically developed within and above root-bearing strata (Fig. 6D). Calcified horizons exhibit a
258 range of development stage, from early stages with thin calcic layers (Fig. 6C) to late stages with
259 complete and dense calcification of the strata (Figs. 6B and 6E).

260 **Footwall strata**

261 Measured footwall stratigraphic sections include the Schoolhouse section (SH) in the east
262 and the Mathews Canyon section (MC) in the west (Figs. 2 and 5). Footwall strata exhibit all
263 depositional facies listed in Table 1. The base of the footwall section is well exposed in SH and is
264 dominated by debris flows (facies C1) and mudflows (facies C3) with interbedded thin weathered
265 basalt and tephra (facies V1 and V2, respectively) (Figs. 5 and 6A). The lower ~50 meters of SH
266 and MC are capped by a ~1-m-thick strongly imbricated conglomeratic layer with a well-defined
267 basal scour (facies C2; Fig. 5). Above this layer, the strata change abruptly to lacustrine siltstone
268 dominated strata (L1-L2) that were deposited in buttress unconformity with the coarser strata
269 below (Fig. 4). The boundary between dominantly colluvial to dominantly lacustrine depositional
270 facies occurs at ~290 meters elevation, which correlates well with the base of the Taunton Ringold
271 section, located to the east (Fig. 7; Packer and Johnson, 1979). Based on interbedded L1 and L2
272 facies strata, we infer a balance-filled lake system wherein fluctuating lake level was common
273 (Olsen, 1990; Carrol and Bohacs, 1999). Because thin conglomeratic layers (facies C2 and C4)
274 interbedded within the lacustrine strata are more common towards the top of the measured strata

275 (Fig. 5), we infer that the lacustrine system became progressively more overfilled with minimal
276 lake fluctuation (Olsen, 1990; Carroll and Bohacs, 1999). The tops of finer layers (facies C2, C4,
277 L1, L2, A1) occasionally show granular structure, root casts, and petrocalcification, which are
278 indicative of periods of landscape stability.

279 From the footwall strata, we collected several samples for U-Pb zircon and U-series age
280 analyses, and for U-Pb zircon provenance analysis. In stratigraphic order, tephra samples for
281 stratigraphic age control are 15SM006, collected at the base of SH, 15SM007, collected within the
282 dominantly conglomeratic section of SH, and 15SM003, collected near the top of the dominantly
283 conglomeratic section of MC, (Fig. 5). We also analyzed one reworked tephra in MC for U-Pb
284 zircon provenance analysis (15SM004). Sample 15SM011 is a collection of calcified root casts
285 sampled at the top of SH for U-series dating.

286 **Hanging wall strata**

287 From east to west, the four stratigraphic sections measured in the hanging wall of the SMF
288 include the Duct tape (DT), Pinnacle (PN), Jericho (JR) and Feedlot (FL) sections (Figs. 2 and 5).
289 These locations were chosen for stratigraphic analysis based on quality of exposure and available
290 age control. Facies L1 and L2 are absent from the hanging wall strata, but all others are present
291 (Table 1). Facies V1 is only present in JR and is capped by a 1.2 m thick lapilli tuff. For facies C1
292 and C3 in the hanging wall strata, conglomerate is more prevalent in the eastern two stratigraphic
293 sections (DT, PN), which is likely because DT and PN sections are situated along the north slope
294 of the Saddle Mountains anticline in a region that would accommodate more detritus from hillslope
295 erosion compared to JR and FL sections (Fig. 2). Conglomeratic strata commonly fine upward into
296 loess-rich deposits with petrocalcic horizons (Fig. 5).

297 A distinctive conglomerate layer is the basis for a key correlation of hanging wall and
298 footwall strata and in turn allows us to calculate vertical separation across the Saddle Mountains
299 fault. Facies C2 is present as the uppermost conglomeratic layer in hanging wall sections DT and
300 PN and is the only closed-framework conglomeratic layer in hanging wall section FL. It is absent
301 from JR (Fig. 5). Because facies C2 is also present as a single layer in the footwall sections SH and
302 MC, we infer that the distinctive facies C2 in the hanging wall and footwall strata are correlated
303 horizons that were originally deposited at the same elevation (Fig. 5).

304 Within the hanging wall facies, we sampled two tephra layers from JR section (15SM002,
305 16SM001). The lowermost sample was taken from directly above the weathered basalt and the
306 uppermost was taken near the top of the JR section, directly below the capping caliche horizon
307 (Fig. 5). One sample was taken of U-Pb zircon provenance analysis, collected from a reworked
308 tephra layer in DT (15SM013) (Fig. 5). The overlying caliche horizon is locally steeply dipping
309 (Fig. 6B) within a hanging wall fold (Fig. 8), suggesting deformation continued after calcification
310 of the petrocalcic horizon. We sampled the deformed caliche layer for U-series age analysis
311 (16SM002, 16SM003; Fig. 5).

312

313 **GEOCHRONOLOGY**

314 **U-Pb zircon geochronology**

315 We analyzed seven samples for U-Pb zircon analysis via laser ablation inductively
316 coupled mass spectrometry (LA-ICP-MS). Five tephra samples were analyzed for age of
317 volcanic eruption (15SM002, 15SM003, 15SM006, 15SM007, 16SM001), one sandstone sample
318 was analyzed for detrital zircon ages (15SM013), and one reworked tephra sample was analyzed

319 for both detrital zircon and volcanic eruption ages (15SM004) (Fig. 5). A detailed explanation
320 methodology of U-Pb zircon age analysis is available in the Appendix.

321 For tephra samples, between 55 and 139 individual zircon crystals were analyzed,
322 depending on the quality of the sample. Geological ages were determined using the maximum
323 number of spot analyses able to define the youngest coherent age group with $n \geq 3$. This follows
324 an approach discussed by Dickinson and Gehrels (2009) to reliably determine the maximum
325 depositional ages of strata. Because the samples investigated here are mostly volcanoclastic, the
326 ages of the youngest major zircon populations are interpreted to be more reliable than age groups
327 with very low N, single youngest grains or 2 grains. Those youngest grains were treated as
328 outliers and possible contamination by strata from higher levels, which is difficult to avoid in
329 semi-consolidated volcanoclastic material.

330 For provenance samples, at least 100 crystals were analyzed for each sample. Detrital
331 zircon age spectra from the Saddle Mountains were compared to datasets available for modern
332 and ancient detrital sediments from the Snake River Plain (Greslins et al., 1999; 2002; Link et
333 al., 2006; Beranek et al., 2006). We compared the coefficient values of cross-correlation,
334 likeness, and similarity based on Kernel Density Estimations (KDEs) of sample ages, and
335 performed Kuiper and Kolmogorov-Smirnov (K-S) tests on detrital zircon datasets using the
336 DZStats v2.0 program for statistical comparison of detrital zircon age spectra (Saylor and
337 Sundell, 2016). Cross-correlation, likeness and similarity values can range between 0 and 1, with
338 higher values representing a better fit between detrital zircon age spectra (Gehrels, 2001; Saylor
339 and Sundell, 2016). K-S and Kuiper p-values of < 0.05 indicate that two age spectra are from
340 different sources, within 95% confidence (Press et al., 1986). Since the number of zircons
341 analyzed from Snake River Plain and Ringold Formation samples is typically < 200 , we used the

342 mean Kuiper and K-S p-values calculated from 5 trials of subsampling and comparison without
343 replacement (Saylor and Sundell, 2016).

344 *Tephra zircon results and interpretation*

345 U-Pb zircon age results for tephra samples collected from the Saddle Mountains provide
346 new age constraints on the timing and rate of sediment accumulation. The results of the individual
347 LA-ICP-MS spot analyses for tephra samples are available in Tables A2–A6. From the hanging
348 wall, we collected two tephra samples from section JR, which provide tephra ages in stratigraphic
349 order (Figs. 5 and 9). For sample 15SM002, we calculate a concordia age of 9.51 ± 0.09 Ma
350 (MSWD=1.5) based on a group of 37 zircons out of the 48 analyses (Fig. 9A). For sample
351 16SM001, stratigraphically above 15SM002, we calculated an age of 6.79 ± 0.07 Ma
352 (MSWD=1.3) from a coherent group of 78 zircons out of the 107 total analyses (Fig. 9B). As
353 mentioned in the Appendix, the reference zircon material analyzed along with sample 16SM001
354 was 2.7% younger than the published age, and so we regard the concordia age of 6.79 ± 0.07 Ma to
355 be a minimum, albeit likely within ca. 3% of the true age of the sample.

356 For footwall samples, all ages occur in stratigraphic order (Figs. 5 and 9). From the lowest
357 sample collected in the Schoolhouse section (15SM006), we calculated a concordia age of $9.51 \pm$
358 0.14 Ma (MSWD=1.2) from a coherent group of 17 zircons out of the 35 concordant zircons
359 analyzed (Fig. 9C). Stratigraphically above 15SM006, results from sample 15SM007 provide a
360 concordia age of 8.06 ± 0.20 Ma (MSWD=1.4) based on a group of 21 zircons (Fig. 9D) from a
361 total of 23 concordant analyses. Sample 15SM003 provides a concordia age of 7.35 ± 0.40 Ma
362 (MSWD=2.2) based on a group of 6 concordant zircons (Fig. 9E). In total, 35 concordant zircon
363 ages were measured for sample 15SM003. From the reworked tephra sample 15SM004, which is
364 the highest tephra sample collected from the footwall, we calculated a concordia age of 3.48 ± 0.11

365 Ma (MSWD=1.3) from the youngest 5 coherent analyses (Fig. 9F). A total of 137 zircons were
366 dated, as this sample was analyzed as a detrital zircon sample.

367 Normalized relative probability plots for tephra samples indicate that samples 15SM002,
368 15SM006, 15SM007 and 16SM001 were minimally reworked, with the vast majority of single-
369 crystal ages falling within a Neogene age peak (Fig. A2). Therefore, we interpret the calculated
370 concordia dates for these samples to represent the timing of volcanic deposition. The broader and
371 less defined young age peak for sample 15SM003 (Fig. A2) indicates that the calculated age may
372 have been more affected by detrital contamination than others, and so we interpret the concordia
373 age of 7.35 ± 0.40 Ma to represent a maximum depositional age for this tephra. Similarly for
374 sample 15SM004, this sample was clearly reworked and the majority of the zircons dated were
375 detrital (Fig. A3). Thus, the 3.48 ± 0.11 Ma concordia age calculated for the youngest 5 analyses
376 represents a maximum depositional age.

377 From the similarity in tephra age and appearance of samples 15SM002 and 15SM006, we
378 interpret these tephra to be correlated horizons across the hanging and footwalls of the SMF (Fig.
379 5). Our U-Pb zircon tephra ages of the lower Ringold Formation establish the age of the base of the
380 unit as 9.51 Ma; the base of the formation is not exposed at the Taunton section and was difficult to
381 date by magnetostratigraphy elsewhere (Packer and Johnson, 1979). The uppermost tephra sample
382 from the footwall strata has an age of 3.48 ± 0.11 Ma, whereas the uppermost tephra sample from
383 the hanging wall is older at 6.79 ± 0.07 Ma (Fig. 5). This may indicate that, in the hanging wall,
384 deposition of the Ringold Formation ceased in the late Miocene, and/or that the preservation of
385 younger Ringold strata is less complete in the hanging wall than in the footwall sections. In
386 summary, our new geochronologic age constraints suggest that the Ringold Formation was
387 deposited between 3.5 and 9.5 Ma. These data are supported by previous magnetostratigraphic

388 analyses of the upper Ringold strata at the Taunton section (Figs. 2 and 7), where Packer and
389 Johnson (1979) suggest lacustrine deposition during the Gilbert Epoch, from 3.596–6.033 Ma
390 using the results from Gradstein et al., 2012.

391 *U-Pb provenance results and interpretation*

392 Since the rock exposed along the SMA is nearly uniformly basaltic, the range of zircon
393 ages and presence of recycled metamorphic minerals indicate that the hanging wall was not
394 uplifted above river level until after the cessation of predominantly conglomeratic deposition.
395 Detrital U-Pb zircons ages for samples 15SM004 and 15SM013 range between 3.3 and 3368 Ma
396 (Fig. A2; Tables A7–A8). As mentioned above, we interpret the concordant Pliocene zircon ages
397 in 15SM004 to represent the timing of deposition, and the older ages to represent reworked
398 fluvial sands. In addition to zircon dating, we identified monazite, rutile, garnet, and multiple
399 zircon habits during mineral separation of these samples, one of which was taken from the hanging
400 wall strata (Fig. 5). These minerals, particularly monazite, indicate that the lower Ringold strata
401 sources material other than basalt, such as primary or reworked felsic igneous or metamorphic
402 rocks.

403 For intersample comparison of detrital datasets from the Ringold strata and from the
404 Snake River Plain (Greslins et al., 1999; 2002; Link et al., 2006; Beranek et al., 2006), the
405 results for cross-correlation, likeness, similarity, Kuiper and K-S tests are reported in Table A9.
406 The cross-correlation, likeness and similarity values between the detrital zircon age spectra
407 measured in the Ringold strata (15SM004, 15SM013) are uniformly high (>0.75) and the Kuiper
408 and K-S p-values are above 0.05 (Table A9). For intersample comparison of Ringold strata with
409 modern and ancient river sands of the Snake River Plain, cross-correlation, likeness and similarity

410 values typically range between 0.1 and 0.8 (Table A9). Mean Kuiper and K-S p-values range
411 between 0.0 and 0.7 (Table A9).

412 Based on our analysis, we find that the source of the Ringold Formation did not change
413 over the sampled interval and a subset of the Snake River Plain samples compare well with the
414 Ringold Formation samples. As mentioned above, samples with mean K-S and Kuiper p-values
415 above 0.05 and with high coefficients of likeness, similarity, and cross correlation are likely
416 derived from the same source terrane (Saylor and Sundell, 2016). The threshold of what is
417 considered a good comparison for likeness, similarity, and cross correlation is somewhat arbitrary
418 and we chose a conservative value of 0.65. Several of the detrital zircon datasets have relatively
419 few zircons ($n < 100$) and require interpretation of intersample comparison coefficients with
420 caution. Therefore we only consider age spectra to be potentially derived from the same source
421 terrane if both K-S and Kuiper p-values are above 0.05 and all cross-correlation, likeness, and
422 similarity coefficients are above 0.65. Based on these criteria, our results indicate that the only
423 Snake River Plain samples statistically similar to our Ringold samples are modern Snake River
424 (M5 and M6), the Pleistocene South Fork of the Snake River (P6), and the Pleistocene Bonanza
425 Bar (P7) (Figs. 10 and A3, Table A9).

426 The most abundant age population peaks that overlap between the Ringold and Snake
427 River Plain samples are the Eocene Challis Volcanic Group and the Cretaceous Idaho Batholith,
428 both of which are exposed primarily north of the Snake River Plain (Figs. 10 and A3). The zircons
429 older than 250 Ma that overlap between Snake River Plain and Ringold samples include
430 Precambrian age groups such as Grenville zircons, which were possibly recycled from central
431 Idaho or the Idaho-Wyoming thrust belt (Stewart et al., 2001), the Yavapai-Mazatzal, which may
432 be recycled from conglomerates in western Wyoming (Janecke et al., 2000), and Wyoming

433 province zircons exposed in western Wyoming near the South Fork of the Snake River (Fig. A3)
434 (Link et al., 2005). Whether the similar age groups and statistical coefficients indicate that the
435 Snake River itself flowed north of the Saddle Mountains during the Miocene is debatable (Fig. 10).

436 **Petrocalcic horizon dating**

437 We analyzed material from petrocalcic soil horizons collected from the Jericho and
438 Schoolhouse stratigraphic sections for U-series age analysis to provide constraints on the timing of
439 deformation along the Saddle Mountains. U-series dating of petrocalcic cements is based on the
440 premise that the authigenic component precipitates from soil water capable of transporting U, but
441 not Th. The pure authigenic cement thus formed contains U with a $^{234}\text{U}/^{238}\text{U}$ isotopic composition
442 identical to that U dissolved in the soil water but no initial Th. With time, ^{230}Th systematically
443 increases due to in-situ decay of ^{234}U , such that a U-series age can be estimated by determining the
444 $^{234}\text{U}/^{238}\text{U}$ and $^{230}\text{Th}/^{238}\text{U}$ activity ratios (AR). A detailed explanation of sample preparation and
445 methods for U-series analysis is available in the Appendix.

446 Sample 15SM011 consists of calcified roots (rhizoliths) collected from the uppermost
447 petrocalcic horizon exposed in the footwall strata (SH; Figs. 5, 6D, and 11A), which is undeformed
448 at the site of collection but possibly correlative to the faulted horizons described in previous
449 paleoseismic research along the SMF (West et al., 1996). Samples 16SM002 and 16SM003 were
450 collected from the uppermost petrocalcic horizon exposed in the hanging wall strata (JR; Fig. 5),
451 which is over 80 cm thick and has been tilted 67° at the site of collection (Fig. 6B). 16SM002 was
452 collected from the lower portion of this calcic horizon where the material is more massively
453 cemented, and 16SM003 was collected from the uppermost beds where thinner pedogenic rinds
454 formed on the undersides of basaltic clasts (Figs. 11B and 11C).

455 ***U-series results and interpretations***

456 The U-series analysis of petrocalcic horizons and calcified rhyzoliths provides the timing of
457 calcification, which we use to interpret the timing of faulting and folding along the Saddle
458 Mountains. Sample 15SM011, collected from the upper portion of the footwall strata, was not
459 deformed at the site of collection but is of the same upper caliche unit faulted in paleoseismic
460 trenches (Fig. 2) (West et al., 1996). We analyzed three root casts and age results range between
461 152–156 ka. Ages are within uncertainty of each other and provide a robust weighted mean age of
462 153.2 ± 3.8 ka (Fig. 11; Table A10). We interpret these results to suggest that this horizon was
463 calcified 153 kyr and that earthquake activity along the Saddle Mountains fault deformed caliche
464 exposed in paleoseismic trenching more recently (West et al., 1996).

465 Samples 16SM002 and 16SM003 were collected from the same petrocalcic horizon in the
466 hanging wall of the SMF, and are distinguished by the nature of calcite formation: 16SM002 is
467 from the massive calcite cement, whereas 16SM003 contains basaltic clasts with calcite rinds
468 (Figs. 11B and 11C). Overall, the results from these samples are not as straightforward as
469 15SM011, with several subsamples not providing interpretable ages due to excess ^{230}Th values or
470 high ^{232}Th values (Table A10). For the subsamples that provide reasonable results, we find that
471 ages range from 79–434 ka for sample 16SM002, and from 45–195 ka for sample 16SM003 (Fig.
472 11). The large range in age results could suggest one of two things: (1) Samples have been
473 diagenetically altered, leading to a depletion of U and preferential enrichment of Th, in which case
474 the calculated ages are not geologically meaningful. (2) Multiple stages of calcite growth have lead
475 to multiple age groups in U-series data.

476 To determine which scenario is most likely, we compare the calculated U-series ages with
477 initial $^{234}\text{U}/^{238}\text{U}$ values. Individually, these samples 16SM002 and 16SM003 do not show a
478 particularly strong correlation between age and Uranium ratios, however taken together, we find

479 that the subsamples with low initial $^{234}\text{U}/^{238}\text{U}$ (between 1.05 and 1.1) are younger and cluster
480 around 100 ka. The remaining subsamples have higher ratios, between 1.3 and 1.5, and older ages
481 (>200 ka). Given the correlation evident in the combined sample ages, we suggest that the sampled
482 horizon has undergone several stages of calcite growth. The age of the first stage is somewhat
483 poorly constrained between 200–400 ka and results show high initial $^{234}\text{U}/^{238}\text{U}$ values. The second
484 pedogenic event, with lower $^{234}\text{U}/^{238}\text{U}$ values, likely occurred between 90–100 ka. The difference
485 in Uranium composition is perhaps due to different climatic conditions and weathering rates during
486 the time of pedogenic carbonate formation.

487 Deformation of the uppermost petrocalcic horizon at JR (Fig. 6B) is due to folding of the
488 hanging wall (Fig. 8), possibly accommodating motion along a lateral ramp at depth. Prior to
489 calcification, the original material of hanging wall and footwall samples consisted of fine loess and
490 was likely friable. The results from samples 16SM002 and 16SM003 show two age groups
491 between 90–100 ka and 200–400 ka. From these data, we suggest that deformation of the horizon
492 postdates the oldest stage calcification and is therefore more recent than 200 ka.

493

494 **STRUCTURAL CROSS SECTIONS**

495 The form of the Saddle Mountain anticline varies along strike and this variation may be
496 strongly influenced by changes in the underlying fault at depth (Suppe, 1985; Rowan and Linares,
497 2000; Allmendinger and Shaw, 2000; Wilkerson et al., 2002). Thus, we constructed two cross
498 sections, A-A' and B-B', to investigate the effect of along-strike changes in fold, and likely fault,
499 geometry (Fig. 2). Both cross sections have a present-day length of 14 km and strike N4°W,
500 parallel to the inferred direction of maximum convergence. To constrain our work, we use

501 geological and geophysical data and combine traditional cross section line-balancing (Dahlstrom,
502 1969) with forward modeling of geophysical anomaly data.

503 Geologic constraints used in cross section construction include new and published
504 structural measurements near cross section transects (Fig. 2; Reidel, 1988), isopach data for
505 stratigraphic thicknesses of CRBG strata (Reidel, 1984) and logged stratigraphy in nearby
506 boreholes BN 1-9, AF 1-6, and Brown 7-24 (Figs. 1 and A1; Wilson et al., 2008; Czajkowski et al.,
507 2012). Borehole locations span the full length of the structural transects and borehole
508 measurements reach up to 5.3 km depth, including both CRBG flow thickness as well as unit
509 thicknesses of the underlying Fifes Peak/Ohanapecosh, Wenatchee, and Roslyn Formations.
510 Isopach data indicate thinning of several Saddle Mountains Basalt members (Reidel, 1984), which
511 is honored in our cross sections, while basalt members remain at constant thickness.

512 Geophysical controls on our structural cross sections include seismic reflection data and
513 high-resolution aeromagnetic anomaly data (Figs. 2 and 12). The seismic profile that elucidates the
514 Saddle Mountains fault geometry was purchased by the U.S. Geological Survey and interpreted
515 previously by Casale and Pratt (2015). Seismic reflections interpreted as bedding orientations reach
516 depths up to 8–10 km. The upper several kilometers of the seismic line are particularly difficult to
517 image because of the CRBG basalt stratigraphy, however interpretable reflectors are apparent in
518 deeper horizons (>2 km depth). Aeromagnetic data, on the other hand, are extremely informative
519 for structures in the Yakima Fold province because of the highly variable magnetic properties of
520 rock types within the region. These include highly magnetized basalts, with both normal and
521 reverse polarity, and essentially non-magnetic overlying and underlying strata (Blakely et al.,
522 2011). The data shown in Figure 12 were acquired in 2008 and 2009 by private consultants under
523 the contract to the U.S. Geological Survey. Blakely et al. (2011) provide a full description of data

524 acquisition and processing procedures. In addition to providing constraints on the cross section
525 results, these aeromagnetic data were used to modify the mapped trace of the Saddle Mountains
526 fault where field observations were lacking by tracing contours in strong horizontal gradients
527 calculated from the magnetic anomaly data (Figs. 2 and 12).

528 **Methods**

529 The surface geology along transects A-A' and B-B' were matched to the geologic mapping
530 of Reidel (1988) and supplemented with new bedding orientations where structural data were
531 originally sparse (Fig. 2). These data were entered into Oasis Montaj, a program for modeling
532 geophysical data, along with the aeromagnetic data and a 10-m resolution digital elevation model
533 of the Saddle Mountains anticline. For our analysis we used the 100-m resolution total field
534 magnetic anomaly data, where the International Geomagnetic Reference Field, updated to the time
535 of flight, was subtracted from the original total field measurements (Fig. 12). Further details on
536 aeromagnetic data processing are available in Blakely et al. (2011). For basaltic flows and
537 overlying strata, we compiled paleomagnetic data and calculated the weighted mean of spherical
538 quantities for inclination and declination in each flow (Packer and Johnson, 1979; Choiniere and
539 Swanson 1979; Hooper et al., 1979; Wells et al., 1989). For the sub-basaltic strata, we adopted
540 magnetic parameters from Blakely et al. (2011). Table 2 includes information on the magnetic
541 parameters used for each unit.

542 Magnetic anomaly data were extracted along each cross section transect for forward
543 modeling in Oasis Montaj. As cross sections were constructed, the resulting magnetic anomalies
544 were calculated and compared to measured magnetic anomaly data. Unit thicknesses were kept
545 constant unless isopach data suggested otherwise (Reidel, 1984) and bedding orientations were
546 matched to available structural data. The upper and lower contacts of each unit were line-balanced

547 using the sinuous bed method (Dahlstrom, 1969). Exceptions to this include the contact between
548 the Pomona and Huntzinger flows and the base of the Roslyn Formation. The Pomona and
549 Huntzinger flows both thin towards the crest of the SMA and are not observed to the north of the
550 anticlinal crest, and therefore cannot be line balanced with the other contacts. We did not line-
551 balance the basal contact of the Roslyn Formation because seismic reflection data indicate that
552 bedding in the Roslyn Formation dips more steeply than overlying strata and likely experienced
553 more shortening prior to deposition of the Wenatchee Formation (Casale and Pratt, 2015).
554 Furthermore, borehole data do not penetrate into deeper strata and so the base of the Roslyn
555 Formation and/or top of the basement is not well constrained near the Saddle Mountains (Fig. A1).

556 **Cross section results and interpretations**

557 The aeromagnetic data extracted across each cross section transect show a notable along-
558 strike variability in magnetic anomalies that correlates to a difference in the surface geology and
559 structure at depth, and cross sections A-A' and B-B' (Fig. 13) are best fits to the geologic and
560 geophysical data. From the finalized cross sections, we calculate an original length for A-A' of
561 15.33 km, giving an overall shortening of 1330 m (9% shortening) since deposition of the CRBG.
562 For cross section B-B', we calculate an original length of 14.96 km and an overall shortening of
563 960 m (6% shortening) since deposition of the CRBG. At the projected location of BN 1-9 on cross
564 section B-B', we estimate a fault depth of 2300 m and a ~450 m thick repeated section of basalt.
565 These values overlap with estimates of fault depth from fractured rock mass and repeated section
566 from basalt geochemistry (Reidel et al., 1989a) providing independent support for our cross section
567 modeling results. Steeper bed orientations in Eocene strata suggest pre-Miocene deformation on
568 the SMA, however the aeromagnetic data, isopach data, and the uniform shortening along each
569 line-balanced layer suggest that the majority of deformation recorded in the CRBG strata, and

570 possibly the Oligocene strata, post-dates the youngest basalt flow, the 10–10.5 Ma Elephant
571 Mountain Member.

572 While shortening in each balanced layer is uniform, the magnitude of slip increases with
573 the age of the unit, from which we infer that the Saddle Mountains anticline is a fault-propagation
574 fold (Suppe, 1985; Suppe and Medwedeff, 1990; Mitra, 1990), similar to other Yakima folds
575 (Miller, 2014). Thus, the amount of slip preserved in the upper units is an underestimate for the
576 total Miocene – present slip history. To avoid underestimating total slip, and in turn slip rate, we
577 measure the total offset from oldest uniformly shortened unit, the Wenatchee Formation. Our
578 estimates for total slip since 10–10.5 Ma are 1712 m along A-A' and 1178 m along B-B'.

579 Given our shortening and slip estimates, our structural models suggest that there is a
580 westward-increasing slip gradient along the SMF. The slip gradient is consistent with large-scale,
581 long-term clockwise rotation in the U.S. Pacific Northwest (Wells et al., 1998; Wells and
582 McCaffrey, 2013). Clockwise rotation and westward-increasing N-S strain rates are ongoing, as
583 evident from modern GPS measurements in the Yakima fold province (McCaffrey et al., 2013;
584 2016). Our new cross sections provide evidence that clockwise rotation could be manifest along a
585 single structure, and not just along a larger array of structures.

586 While the upper crustal structure of the Saddle Mountains varies along strike, the SMF
587 likely merges at depth to a common fault plane geometry. In our structural model, this occurs at
588 depths between 6 and 7 km (Figs. 13 and 14). We posit that one or perhaps multiple lateral ramps
589 accommodate the along-strike variation (Fig. 14). Several lines of evidence support this
590 interpretation. First, minor apparent right lateral offset on the Smyrna fault, near the Mathews
591 Canyon section (Fig. 2), displaces CRBG flows by tens of meters, so there is certainly some
592 amount of oblique dextral motion on fault step-overs. Furthermore, hanging wall fold axes near the

593 Jericho and Pinnacle sections (Fig. 8) are orthogonal to the large-scale trend of the SMA and may
594 indicate the presence of a lateral ramp at depth (Wilkerson et al., 2002).

595

596 **DISCUSSION**

597 **Timing and rates of deformation and landscape evolution**

598 *Miocene – Pliocene structural and stratigraphic evolution of the Saddle Mountains*

599 With new and published stratigraphic, structural, and geochronologic constraints we
600 reconstruct the geologic history of the Saddle Mountains. The onset of deformation likely predates
601 the late Eocene–Oligocene deposition of the Fifes Peak/Ohanapecosh and Wenatchee Formations
602 based on the steepening of bedding orientations within the Roslyn Formation (Casale and Pratt,
603 2015). Based on the uniform magnitude of shortening preserved in post-Roslyn Formation strata,
604 we infer that there was paucity of deformation from 45 Ma until at least 10 Ma along the SMA.
605 Slight thinning of several basalt flows near the crest of the SMA may suggest that minor anticlinal
606 growth occurred between ~16–11 Ma (Reidel, 1984), but we establish from our cross section
607 results that deformation at this time is relatively minor to the overall shortening accommodated
608 along the SMA. Our new tephra U-Pb zircon age results indicate that the onset of Ringold
609 Formation deposition was ca. 9.5 Ma and that deposition ceased shortly after 3.5 Ma. The initiation
610 of debris flow and mudflow deposition in the lower Ringold Formation at 9.5 Ma signals relief
611 generation across the Saddle Mountains by this time. We therefore suggest the onset of renewed
612 deformation along the SMA between 10 and 9.5 Ma. Stratigraphic observations and tephra dating
613 indicate that deposition of debris flow and mudflow continued throughout the late Miocene and
614 into the Pliocene (until at least 3.5 Ma), which we interpret as continued anticlinal growth, relief
615 generation and hillslope erosion.

616 Stratigraphic observations also allow us to characterize Miocene–Pliocene deformation
617 along the SMA. The upper boundary of conglomerate-dominated strata in the hanging wall
618 sections is marked by a fluvial channel fill horizon, below which we find detrital zircon grains with
619 distal provenance similar to that of the Snake River Plain. This indicates that the hanging wall
620 remained at river level for some time. However, the strata in the hanging wall and footwall become
621 dissimilar after the fluvial channel fill horizon. In the footwall, there is a shift from dominantly
622 conglomeratic deposition to dominantly lacustrine deposition with interbedded mudflow and debris
623 flow facies (Fig. 5), whereas in the hanging wall lacustrine strata are absent from (Fig. 5). We infer
624 that the hanging wall was uplifted above lake level by the time lacustrine deposition initiated and
625 that the appearance of lacustrine strata in the footwall suggests that rivers were diverted away from
626 the north side of the Saddle Mountains.

627 Concurrent with the lithostratigraphic shift, the footwall strata change from displaying
628 fanning bedding dip orientations to displaying uniformly subhorizontal bedding (Fig. 4). Fanning
629 dips we observe in the lower Ringold formation are typical of growth strata (Suppe et al., 1992),
630 and provide further evidence for syndepositional deformation in the footwall sections. The change
631 to subhorizontal bedding suggests that the footwall was no longer tilted during deposition. We
632 therefore suggest that the change from fanning to subhorizontal dips represents the time at which
633 the Saddle Mountains fault propagated to the surface, otherwise termed a fault breakout
634 (Allmendinger, 1998).

635 *Age estimate for channel fill marker bed*

636 From our stratigraphic observations of the Ringold Formation near the Saddle Mountains
637 anticline, we identified a unique channel fill horizon present in the majority of our measured
638 sections (Fig. 5). Estimating the age of this horizon is essential for understanding deformation

639 history of the SMA for two reasons: First, this horizon, along with the 10–10.5 Ma Elephant
640 Mountain Member, allows us to estimate the timing and rate of deformation (further discussed
641 below). Second, this horizon forms the boundary between the lower Ringold Formation, where
642 beds have fanning dips typical of growth strata (Suppe et al., 1992), and the upper Ringold
643 Formation, where strata are subhorizontal (Fig. 4). Thus, the marker bed age provides an important
644 constraint on the timing of fault breakout (Allmendinger, 1998).

645 To estimate the age of the marker bed, we assess the tephra ages from the footwall strata
646 and their relative stratigraphic position. Given the linear relationship between stratigraphic position
647 and tephra age, we are able fit a simple linear regression through this data and calculate that the
648 channel fill marker bed was deposited at 6.81 ± 0.27 Ma (Fig. 15). We suggest, then, that the
649 Saddle Mountains fault propagated to the surface soon after the deposition of the ca. 6.8 Ma
650 marker horizon. Fault breakout at this time provides evidence of a tectonic mechanism for the
651 dramatic change to dominantly lacustrine strata in the upper Ringold Formation. We propose that
652 propagation of the SMF to the surface ca. 6.8 Ma may have diverted the fluvial system,
653 stratigraphically represented in the lower Ringold Formation, away from the actively growing
654 anticline, creating a shallow lake system near the Saddle Mountains that persisted until 3.5 Ma.
655 Based on the lack of lacustrine strata in the hanging wall (Fig. 5), we infer that enough relief was
656 generated across the anticline after fault breakout to preclude lacustrine deposition in the hanging
657 wall sections. Additionally, while the estimated 6.8 Ma age for the marker bed and the 6.79 ± 0.07
658 Ma age for the uppermost hanging wall tephra (16SM001) are within uncertainty, the lack of
659 channel fill deposition in section JR precludes our correlation between footwall strata and hanging
660 wall strata at JR (Fig. 5). The absent marker bed in JR section may be from lack of preservation or
661 from localized relief above river level at ~ 6.8 Ma. The proximity of section JR to a small anticlinal

662 crest in the hanging wall provides a mechanism for localized relief at this particular locality (Fig.
663 2).

664 *Relief generation and spatiotemporal variation in the deformation rate*

665 The presence of two marker beds in Miocene basaltic and suprabasaltic strata give us the
666 unique opportunity to estimate the magnitude of structural relief generated across the SMA over
667 time (Suppe et al., 1992). We reconstruct the magnitude of structural relief generated by 6.8 Ma
668 using the difference in the thickness of strata between the 10–10.5 Ma Elephant Mountain Member
669 and the 6.8 Ma marker bed (Fig. 16). The stratigraphic separation between the Elephant Mountain
670 Member and the channel fill marker bed in the footwall (T_F) varies from 50–54 meters, which we
671 average to 52 meters (Figs. 5 and 16). The stratigraphic separation between these two marker
672 horizons in the hanging wall (T_H), on the other hand, ranges between 10 and 29 meters (Fig. 5).
673 The Pinnacle Section (PN) is nearly identical in lithostratigraphy but more complete than the
674 nearby Duct Tape Section (DS), from which we posit that localized relief has reduced the
675 stratigraphic separation in DS (Fig. 5). We therefore only consider stratigraphic separations
676 between the Elephant Mountain Member and the channel fill marker bed (T_H) from sections PN
677 and FL in the hanging wall, which are 24 and 29 m respectively (Fig. 5). From the difference
678 between T_F and T_H , we calculate that, from 10–10.5 and 6.8 Ma, there were 28 meters of structural
679 relief generated on the SMA at PN and 23 meters of structural relief generated along the SMA near
680 FL (Fig. 16). The magnitude of structural relief generated across the SMA since 6.8 Ma is much
681 greater, varying from 187 meters in the east (PN) to 287 meters in the west (JR) (Fig. 16).

682 The structural relief generated, equivalent to relative rock uplift, along the SMA over these
683 two periods of time allows us to calculate the rate of deformation and how it varies spatially and
684 temporally. Between 10–10.5 and 6.8 Ma, the rate of relative rock uplift along the SMA was <0.01

685 mm yr⁻¹. The average rate after 6.8 Ma is up to six times greater than the previous rate, ranging
686 between 0.04 mm yr⁻¹ in the west and 0.02 mm yr⁻¹ in the east. The spatial variation in uplift rates is
687 consistent with the results from our structural cross sections that show an overall westward-
688 increasing slip gradient along the SMF. Given the magnitude of shortening and slip we established
689 in our cross sections along the Saddle Mountains fault (Fig. 13), we calculate that the shortening
690 rate between 10–10.5 and 6.8 Ma was 0.03–0.04 mm yr⁻¹ and that the rate of slip during this same
691 time was 0.04–0.05 mm yr⁻¹. Since 6.8 Ma, the shortening rate increased to 0.18 mm yr⁻¹ in the
692 west and 0.12 mm yr⁻¹ in the east. For this same time period, the slip rate increased to 0.23 mm yr⁻¹
693 in the west and 0.15 mm yr⁻¹ in the east. Because the rock uplift rates between 10–10.5 and 6.8 Ma
694 are low and within uncertainty of each other, we are unable to assess from our data whether this E-
695 W deformation gradient was established before 6.8 Ma.

696 Previous studies on rotation of the magmatic arc indicate that clockwise rotation of the U.S.
697 Pacific Northwest was established by 16 Ma (Wells and McCaffrey, 2013). Since the westward
698 increasing cumulative deformation of along the SMA mimics the long-term, regional clockwise
699 rotation, this could suggest that the slip gradient along the SMF was established early in the uplift
700 history. If the slip gradient has been a consistent and long-term character of the Saddle Mountains,
701 we would expect the geomorphology across the SMA to be similarly adjusted to the deformation
702 rate. Another possibility is that the slip gradient along the SMA is a product of eastward lateral fold
703 propagation, from which we would expect to see an eastward decrease in drainage density and
704 ridge dissection, as this would be a structurally and geomorphically young region of the fold
705 (Keller et al., 1999). Geomorphically, however, the landscape along the western portion of the
706 Saddle Mountains appears younger than the eastern portion. Therefore, we suggest that the
707 decreased drainage density and ridge dissection along the western portion of the fold may indicate

708 that the landscape has not fully adjusted to the 6.8 Ma increase in uplift rate, and that the slip
709 gradient along the SMF was established recently (≤ 6.8 Ma). A young establishment of this slip
710 gradient is not mutually exclusive with the onset of clockwise rotation in the Pacific Northwest by
711 ~ 16 Ma, and is only indicative of how the observed clockwise rotation is resolved along individual
712 faults and folds in the Yakima fold province.

713 The deformation gradient we interpret from stratigraphic and structural data likely
714 continues, with shortening increasing to the west of transect A-A' and decreasing to the east of
715 transect B-B'. Based on the series of fold axes orthogonal to the main trend of the SMA (Fig. 8)
716 and NW-SE trending lateral faults mapped and inferred (Fig. 2; Reidel, 1988), we posit that the
717 fault-normal slip gradient is, at least partially, accommodated by a series of lateral structures, rather
718 than simply oblique slip along the main Saddle Mountains fault plane. Broadly, paleomagnetic
719 measurements along the Saddle Mountains show between 10° and 15° of clockwise rotation in the
720 hanging wall of the SMF since the mid Miocene, in comparison to only $\sim 5^\circ$ in the footwall (Fig.
721 A4) (Reidel et al., 1984). The exception to this is localized area of increased clockwise rotation
722 along the Saddle Gap segment of the SMA (Reidel et al., 1984). We attribute the localized increase
723 of clockwise rotation to a southward bend in the SMA (Fig. A4). Together, the slip gradient
724 observed in structural data and paleomagnetic datasets suggest clockwise rotation has been
725 accommodated along the SMF since Miocene time.

726 *Late Pleistocene to modern deformation*

727 Several lines of evidence indicate that deformation along the Saddle Mountains continues
728 today. Using U-series analysis, we date the youngest deformed units exposed: ages from a steeply
729 tilted petrocalcic horizon indicate that deformation has certainly persisted until at latest 200–400
730 ka, and faulted petrocalcic horizons are perhaps as young as 153 ka (Figs. 6B and 11).

731 Furthermore, modern seismicity in the Yakima fold province clusters along the SMF and
732 epicenters are distributed along the entire length of the anticline, from the eastern Saddle
733 Mountains to the western Boyleston Mountains, and even into Kittitas Valley (Fig. 1).
734 Unfortunately, we cannot determine a rate of deformation along the SMA from the dated
735 petrocalcic horizons nor from the geodetic data (McCaffrey et al., 2016). While the modern rate of
736 deformation along the Saddle Mountains cannot be determined from the currently available data,
737 we can evaluate the long-term deformation rates along the SMA in relation to the modern,
738 geodetically measured, deformation across the entire Yakima fold province. A central assumption
739 in our comparison is that the regional geodetic shortening rate has been sustained over the past 6.8
740 Myr, which is an untested hypothesis and is discussed further below.

741 When compared to geodetic rate of deformation, we find that the average shortening rate
742 accommodated across the SMA since 6.8 Ma ($0.12\text{--}0.18\text{ mm yr}^{-1}$) is between 7–11% of the
743 geodetic rate of regional north-south shortening measured between latitudes -120.1°E and -119.1°E
744 ($\sim 1.67\text{ mm yr}^{-1}$; McCaffrey et al., 2016). If we assume that the deformation rate along the SMA
745 has remained constant since 6.8 Ma, then the vast majority of the shortening measured in the
746 Yakima fold province is taken up along other structures either to the north or south of the Saddle
747 Mountains. However, several lines of evidence may suggest that the rate of deformation currently
748 accommodated along the SMA is greater than the long-term trend determined from Miocene strata.

749 Paleoseismic work along the Saddle Mountains suggests that the late Quaternary to modern
750 rate of slip along the SMF is between $0.33\text{--}0.65\text{ mm yr}^{-1}$ (West et al., 1996), about 2–3 times
751 greater than our calculated rate since 6.8 Ma and, accordingly, about 24–30% of the geodetic rate
752 (McCaffrey et al., 2016). Additionally, there are only a handful of other Yakima folds that likely
753 accommodate north-south shortening between -120.1°E and -119.1°E , including the Frenchman

754 Hills anticline, the Rattlesnake Hills anticline, and the Gable Mountains which are the eastward
755 extension of the Umtanum anticline. GPS measurements are unable to detect shortening across any
756 of these, or other, individual structures. Therefore it is unlikely that any one structure
757 accommodates the majority of the modern shortening. Lastly, the Saddle Mountains are
758 topographically more prominent than these other folds and display much more seismic activity
759 (Fig. 1). Together, these data indicate that the SMA continues to be an important tectonic structure
760 that accommodates a component of the active north-south shortening and that the rate of
761 deformation accommodated along the Saddle Mountains has continued to increase over geologic
762 time.

763 **Implications for seismic hazard in central Washington**

764 Our estimates of the geometry and slip rate for the SMF allow us to place some constraints
765 on the seismic hazard posed by the SMF by quantifying the time required to accumulate enough
766 strain energy to produce moderate to large earthquakes along the Saddle Mountains fault. This time
767 interval may be broadly interpreted as a proxy for recurrence intervals for earthquakes of some
768 magnitude, given a few assumptions discussed below. We calculate the strain accumulation time t
769 as $t = M_o \sin \delta / (\mu L z \dot{s})$, where M_o = seismic moment, δ = dip, μ = shear modulus, L = fault
770 length, z = seismogenic thickness, and \dot{s} = fault slip rate. We convert M_o to moment magnitude
771 M with the relation $M = 2/3 \log_{10}(M_o) - 6$ (Aki and Richards, 2002). From our cross section,
772 geologic mapping, and the modern seismicity near the Saddle Mountains, we estimate the SMF dip
773 δ at 37° , the fault length L is ~ 116 km, and earthquakes rupture at depths z down to 18 km. In our
774 calculations, we use two different slip rates: one from the new geologic data presented in this work
775 and another from paleoseismic work (West et al., 1996). We provide both estimates because of the
776 possible uncertainties associated with each fault slip rate estimate. For instance, we suggest in the

777 preceding discussion that the rate of deformation along the SMA has increased since 6.8 Ma, and
778 so the slip rate derived from the geologic data may be a lower bound on the modern slip rate. The
779 higher slip rate derived from paleoseismic data may be uncertain if the paleoseismic record
780 underestimates or overestimates the number and/or magnitude of earthquakes accommodated along
781 the SMF (McCalpin and Nelson, 1996). The calculated curves displayed in Figure 17 show the
782 time required to accumulate sufficient strain along the SMF to cause earthquakes of a given
783 magnitude, with associated uncertainty resulting from slip rate uncertainties. We note that these
784 curves are not frequency-magnitude distributions, but instead represent the time between an
785 earthquake and the next of the specified magnitude.

786 Interpreting these results as proxies for recurrence interval rests on several important
787 assumptions. The first major assumption is that the strain accumulated on the entirety of the SMF
788 is seismically released during an earthquake. Any aseismic strain release would linearly change the
789 results on Figure 17. For example, if 50% of the elastic strain was released aseismically, then the
790 calculated earthquake recurrence rate would be twice that of the values shown in Figure 17.
791 Aseismic creep has not been identified on the SMF, or any of the Yakima folds, and therefore
792 suggest that aseismic strain is minor if at all present. The second major assumption is that each
793 earthquake will release all of the accumulated elastic strain, so that the time until the next
794 earthquake determines the second earthquake's magnitude. However, we know that lower-
795 magnitude earthquakes occur along the SMF (Fig. 1), so the recurrence intervals of high-
796 magnitude earthquakes along the SMF are likely longer than the values in Figure 17. That said,
797 historic earthquakes near and on the SMF are generally $M < 3$ (Fig. 1) and rupture only a small area.
798 Thus, the amount of energy released by smaller earthquakes is minor compared to the accumulated
799 strain along the SMF. Given these assumptions and their implications, we interpret our calculated

800 seismicity curves to represent a slight underestimate of the time required to generate a large
801 magnitude earthquake, but are generally within the correct order of magnitude.

802 Given the spatial extent of the SMF, it is capable of generating earthquakes exceeding M7
803 (West et al., 1996; Casale and Pratt, 2015). If the Saddle Mountains fault only produces M5–6.5
804 magnitude earthquakes, we calculate that these would rupture on centennial to even annual
805 timescales and be expected to have occurred historically (Fig. 17B). But because M5–6.5
806 earthquakes have not been observed historically, we suggest that the SMF is accumulating strain to
807 be released during a larger event. Large-magnitude ruptures are found in the paleoseismic record,
808 which shows that the most recent earthquake along the SMF produced up to 6.5 meters of vertical
809 offset (West et al., 1996).

810 Based on the slip rate we establish from 6.8–0 Ma, we estimate that a M7 earthquake
811 would rupture every 1.6–2.0 kyr, or that a M7.5 would rupture every 7–11 kyr (Fig. 17A). With the
812 paleoseismically established slip rate from West et al. (1996), we calculate that an M7 earthquake
813 would rupture every 0.5–1.0 kyr, or that a M7.5 would rupture every 2.5–5.0 kyr (Fig. 17A).
814 Overall, we find that large magnitude earthquakes could rupture along the SMF every 2–11 kyr.
815 The paleoseismic record, on the other hand, suggests that large magnitude earthquakes have not
816 ruptured along the SMF since at least 20 kyr (West et al., 1996). This may indicate that the
817 paleoseismic catalog is incomplete, which is a strong possibility given that large magnitude
818 earthquakes do not always rupture the surface and that the trenches excavated along the SMF were
819 not on the actual fault trace, but rather of an ancillary structure in the hanging wall (West et al.,
820 1996).

821 Given the seismic hazard implications from this work, the concentration of seismic activity
822 along the SMA, its topographic prominence, and the accelerating deformation rate, we suggest that

823 the Saddle Mountains pose a seismic hazard to surrounding communities and infrastructure.
824 Should a large magnitude earthquake rupture the SMF, several population centers, including
825 Ellensburg, Yakima, and the Tri-Cities area (Richland, Pasco, and Kennewick), as well as nearby
826 infrastructure (most importantly the Hanford Site and several large hydroelectric dams on the
827 Columbia River) would experience strong ground shaking (Fig. 1). Lastly, geodetic data suggest
828 that the Saddle Mountains accommodate only some of the measured shortening, and that other
829 faults-cored anticlines in the Yakima fold province accommodate the remaining 70–90% of strain
830 energy and may be similarly capable of producing large magnitude earthquakes.

831

832 **CONCLUSIONS**

833 Our stratigraphic, structural, and geochronologic work in central Washington documents
834 the history of deformation and drainage reorganization along the Saddle Mountains anticline and
835 places important constraints on regional seismic hazards. From detailed structural and geophysical
836 models along the Saddle Mountains, we find that shortening accommodated within the CRBG has
837 occurred since 10 Ma and that there is a westward-increasing slip gradient along the Saddle
838 Mountains fault. This is consistent with large-scale clockwise rotation of the U.S. Pacific
839 Northwest and suggests that vertical axis rotation is accommodated along individual faults. We
840 find that the fluvial strata within the Ringold Formation were sourced from central Idaho since the
841 late Miocene, with a similar source terrane as the modern-Pleistocene Snake River. Based on our
842 stratigraphic and structural analysis of the growth strata preserved within the Ringold Formation,
843 we document a previously unrecognized increase in the rate of shortening and slip accommodated
844 along the Saddle Mountains fault. We estimate that the average slip rate since 6.8 Ma ranges from
845 0.15 mm yr⁻¹ in the east to 0.23 mm yr⁻¹ in the west. If this slip rate has been constant since 6.8 Ma,

846 we calculate that the time required to accumulate enough strain energy for a large magnitude
847 earthquake ($M \geq 7$) along the Saddle Mountains fault is between 2 and 11 kyr. We note that our N-S
848 shortening estimate is only 7–10% of the measured geodetic shortening across northern Oregon
849 and central Washington, suggesting that earthquake hazards posed by the Saddle Mountains faults
850 only constitute a fraction of the total regional hazard.

851

852 **APPENDIX**

853 **U-Pb Zircon Geochronology Methods**

854 To analyze samples for tephra and detrital zircon age dating, zircons were separated from
855 crushed samples using standard heavy-mineral separation techniques including a disk mill,
856 GEMENI[®] table, Frantz[™] isodynamic magnetic separator and heavy liquids (methylene iodide).
857 For tephra samples, zircon grains were handpicked under a binocular microscope. For detrital
858 zircon samples, representative splits were obtained with a microsplitter. Zircons were mounted
859 on slides with double-sided tape and analyzed without polishing in order to obtain ages from the
860 outermost portion of the crystal in case of zoning.

861 All samples (15SM002, 15SM003, 15SM004, 15SM006, 15SM007, 15SM013, and
862 16SM001) were analyzed at the University of Kansas Department of Geology using a Thermo
863 Scientific Element2 ICP-MS attached to a Photon Machines Analyte.G2 193 nm ArF excimer
864 laser ablation system. Laser ablation of 20 μm circular spots were obtained at 2.0 J cm^{-2} fluency
865 and a 10 Hz repetition rate, resulting in $\sim 15 \mu\text{m}$ deep pits. The ablated material was carried to the
866 ICP in He gas with a flow rate of 1.1 l/min and tied in with Ar gas, also with a flow rate of 1.1
867 l/min, $\sim 25 \text{ cm}$ before entry into the plasma torch. Two to three natural zircon reference material
868 standards were used for calibration and accuracy checks (GJ1 for calibration, Plešovice or Fish

869 Canyon tuff). Elemental fractionation, downhole fractionation and calibration drift were
870 corrected by bracketing measurements of unknowns with the GJ1 reference material (Jackson et
871 al., 2004) and data reduction using the VizualAge data reduction scheme (Petrus and Kamber,
872 2012) for the IOLITE software package (Paton et al., 2010; 2011). Two-sigma uncertainty for
873 single spots on the GJ1 zircon standard typically range between 0.8% and 2.2% of the U-Pb age
874 and were propagated into the uncertainty of unknowns (Table A1). The zircon Plešovice
875 reference material (Sláma et al., 2008) yielded a weighted mean $^{206}\text{Pb}/^{238}\text{U}$ dates within 2% of
876 the 337.13 ± 0.37 Ma age determined by chemical abrasion thermal ionization mass
877 spectrometry (CA-TIMS, Sláma et al., 2008; Table A1). The zircon Fish Canyon tuff reference
878 material (Schmitz and Bowring, 2001) yielded a weighted mean $^{206}\text{Pb}/^{238}\text{U}$ dates within 0.8% of
879 the 28.476 ± 0.029 Ma age determined by ID-TIMS for most U-Pb analytical sessions (Schmitz
880 and Bowring, 2001; Table A1). However, for the analytical session of sample 16SM001, the Fish
881 Canyon tuff reference zircons yielded an age of 27.74 ± 0.21 Ma, which does not overlap with
882 the uncertainty of the published ID-TIMS age (Schmitz and Bowring, 2001; Table A1), but is
883 just outside of a 2% reproducibility envelope. Therefore, the measured zircon U-Pb dates for
884 sample 16SM001 are considered precise, but may not be as accurate as the other age
885 determination. This possibly renders the resulting age ca. 2-3% younger than the true age of
886 volcanic eruption. We therefore consider the measured U-Pb zircon age for 16SM001 to be a
887 minimum.

888 We used the $^{207}\text{Pb}/^{206}\text{Pb}$ date to estimate the geological age of a grain for $^{206}\text{Pb}/^{238}\text{U}$ dates
889 older than 1000 Ma. Single spot analyses older than 1000 Ma were considered concordant and
890 used in age determinations if the calculated discordance% obtained was lower than $\pm 5\%$. For
891 analyses with $^{206}\text{Pb}/^{238}\text{U}$ dates younger than 1000 Ma an uncertainty weighted discordance

892 (UWD) was calculated as the difference between the $^{207}\text{Pb}/^{235}\text{U}$ and the $^{206}\text{Pb}/^{238}\text{U}$ dates divided
893 by the uncertainty on the $^{207}\text{Pb}/^{235}\text{U}$ date. All analyses with UWD higher than ± 1.2 were
894 interpreted as discordant. Data thus determined as discordant, data with large analytical errors
895 ($^{207}\text{Pb}/^{235}\text{U}$ age uncertainty > 5 Ma) and/or analyses with durations shorter than 8 seconds were
896 omitted from tephra age calculations to focus the age calculations on the most accurate and
897 reliable analytical data. Concordia plots and concordia ages for all data were derived using the
898 ISOPLOT software (Ludwig, 2003).

899 **U-Series Geochronology Methods**

900 Pedogenic material typically includes detrital clays, silts, or sand that contain ^{232}Th , and
901 some ^{230}Th , that is not related to in-situ ^{234}U decay. Therefore, components containing detrital
902 ^{230}Th must be identified and removed as much as possible prior to analysis, or accounted for using
903 ^{232}Th as a monitor of detrital contamination. Calcified roots were mechanically cleaned using
904 carbide rotary dental burs to remove visible detritus adhering to the exterior of rhyzoliths (Fig.
905 11A). Calcic rinds or stringers within the cemented matrix were sampled using 1-mm-diameter
906 dental burs to remove soft or detrital-rich material for the same purpose of reducing ^{230}Th from
907 detrital sources (Figs. 11B and 11C). Once cleaned, subsamples from multiple roots and
908 pedogenic rinds from each unit were obtained by milling with a small dental drill and the resulting
909 powder was collected for isotopic analyses. Ideally, results for aliquots from the same unit will
910 have similar ages increasing confidence that calcification represents a single pedogenic event.

911 Rhyzoliths and rind aliquots were weighed and spiked with a high-purity mixed isotope
912 tracer that contains a known amount of isotopes ^{236}U - ^{233}U - ^{229}Th . Samples were digested at 1 atm
913 and temperatures between 105°C and 125°C with nitric and hydrochloric acid in Teflon™
914 perfluoroalkoxy (PFA) copolymer resin vials. The carbonate components are dissolved in this step

915 but any authigenic opal or detrital silicate material remains undissolved. To avoid laboratory
916 fractionation of U and Th and erroneous $^{230}\text{Th}/\text{U}$ ages, any remaining residue was separated and
917 digested in hydrofluoric acid, then recombined with the original solute. The resulting analyses thus
918 represent total digestion and $^{230}\text{Th}/^{238}\text{U}$ measurements accurately represent values inherent in the
919 subsamples. U and Th were purified using standard ion chromatographic methods with using
920 BioradTM AG1x8 (200-400 mesh) resin. The separated U salts were loaded on rhenium double-
921 filament assemblies, whereas Th salts were loaded on single rhenium filaments sandwiched
922 between layers of graphite suspension. Isotopic ratios were obtained on a Thermo Finnigan
923 TritonTM thermal ionization mass spectrometer equipped with a retarding potential quadrupole
924 electrostatic (RPQ) filter and a single ETPTM discrete-dynode electron multiplier operating in peak-
925 jumping mode. Measured $^{234}\text{U}/^{235}\text{U}$, $^{236}\text{U}/^{235}\text{U}$, $^{230}\text{Th}/^{229}\text{Th}$, and $^{232}\text{Th}/^{229}\text{Th}$ were corrected for
926 mass fractionation, spike contribution, and procedural blank addition, and were normalized relative
927 to an $^{234}\text{U}/^{238}\text{U}$ atomic ratio value of 0.0000529 obtained from National Institute of Standards and
928 Technology (NIST) U-standard SRM4321 measured along with samples. Reported values for
929 $^{234}\text{U}/^{238}\text{U}$ AR were derived from measured $^{234}\text{U}/^{235}\text{U}$ atom ratios assuming a $^{234}\text{U}/^{238}\text{U}$ atom ratio
930 of 137.88 (Steiger and Jäger, 1977).

931 $^{230}\text{Th}/\text{U}$ ages and initial isotopic ratios for individual subsamples were calculated after
932 mathematically removing contributions from a detrital component (Ludwig and Titterton, 1994;
933 Ludwig and Paces, 2002). Detritus-corrected $^{230}\text{Th}/^{238}\text{U}$ and $^{234}\text{U}/^{238}\text{U}$ activity ratios (AR) were
934 obtained using measured $^{232}\text{Th}/^{238}\text{U}$ AR values and the assumptions that the detritus has a uniform
935 U/Th composition similar to average continental crust (Shaw et al., 1976; Taylor and McLennan,
936 1985; Rudnick and Gao, 2003), and is in radioactive secular equilibrium (that is, a composition of
937 $^{230}\text{Th}/^{238}\text{U}$ AR = 1.276 ± 0.64; $^{230}\text{Th}/^{238}\text{U}$ AR = 1.0 ± 0.25; $^{234}\text{U}/^{238}\text{U}$ AR = 1.0 ± 0.1). Uncertainties

938 are propagated through the age calculation such that errors are only slightly larger than those
939 derived solely from analytical uncertainties if measured $^{232}\text{Th}/^{238}\text{U}$ AR is negligible (say $\ll 0.1$);
940 but may be much larger if substantial amounts of ^{232}Th are present (i.e., $^{232}\text{Th}/^{238}\text{U}$ AR > 0.2). Ages
941 and initial ratios were calculated using routines in the program Isoplot/Ex (Ludwig, 2012) and
942 decay constants for ^{234}U and ^{230}Th from Cheng et al. (2013). Measured activity ratios, detritus-
943 corrected activity ratios, and finite ages given by the first-derivative age solutions are reported in
944 Table A10. Uncertainties are reported at the $2\text{-}\sigma$ level and include errors associated with analytical
945 counting statistics, reproducibility from analyses of standards, and uncertainty propagated from
946 any detrital component present. Additional information on standard operating procedure USGS-
947 DRIL-01, R0 Uranium-Thorium Disequilibrium Studies for U-series age analysis is available at
948 http://esp.cr.usgs.gov/projects/uth/USGS_DRIL_01cR0_U_series.pdf.

949 Several standards of known age, including a sample of 69.3-Ma uranium ore in U-series
950 secular equilibrium (Ludwig et al. 1985) and a 119.6 ± 1.9 ka coral dating standard (Watanabe and
951 Nakai, 2006), were run along with unknown samples to ensure data quality. Measured and known
952 standard isotopic ratios are available in Table A11.

953

954 **Acknowledgments**

955 This work was supported by the USGS Mendenhall Fellowship awarded to Staisch. We thank Ray
956 Wells and Gabriele Casale for their thoughtful reviews. We also thank Ethan Hyland, Scott
957 Bennett, John Lasher, and Barbara Brim for their assistance in the field. We appreciate the access
958 granted to us by landowners, especially Gary and Nathan Maughan for road access. Any use of
959 trade, firm, or product names is for descriptive purposes only and does not imply endorsement by
960 the U.S. Government.

961

962 **REFERENCES**

963 Aki, K., and Richards, P.G, 2002, Quantitative seismology. v. 1, University Science Books,
964 Sausalito, CA, p. 700.

965 Allmendinger, R.W., and Shaw, J.H., 2000, Estimation of fault propagation distance from fold
966 shape: Implications for earthquake hazard assessment: *Geology*, v. 28, p. 1099-1102.

967 Allmendinger, R.W., 1998, Inverse and forward numerical modeling of trishear fault-propagation
968 folds: *Tectonics*, v.17. p. 640-656.

969 Barry, T. L., Kelley, S. P., Reidel, S. P., Camp, V. E., Self, S., Jarboe, N. A., Duncan R. A. and
970 Renne, P. R., 2013, Eruption chronology of the Columbia River Basalt Group, *in* Reidel,
971 S.P., Camp, V.E., Ross, M.E., Wolff, J.A., Martin B.S., Tolan, T.L., and Wells, R.E.,
972 eds., *The Columbia River Flood Basalt Province: Geological Society of America Special*
973 *Paper 497*, p. 45-66, doi:10.1130/2013.2497(02).

974 Benjamin and Associates, URS Corporation, Geomatrix Consultants, and Shannon & Wilson,
975 2012, Probabilistic Seismic Hazard Analyses Project for the mid-Columbia Dams:
976 Prepared for Public Utilities Districts of Chelan, Douglas, and Grant Counties, 344 pp.

977 Bentley, R.D., 1977, Stratigraphy of the Yakima Basalts and Structural Evolution of the Yakima
978 Ridges in the Western Columbia Plateau (E. H. Brown & R. C. Ellis, Eds.): *Geological*
979 *Society of America Field Guides*, p. 339–389.

980 Beranek, L.P., Link, P.K., and Fanning, C.M., 2006, Miocene to Holocene landscape evolution of
981 the western Snake River Plain region, Idaho: Using the SHRIMP detrital zircon provenance
982 record to track eastward migration of the Yellowstone hotspot: *Bulletin of the Geological*
983 *Society of America*, v. 118, p. 1027–1050, doi: 10.1130/B25896.1.

984 Blakely, R.J., Sherrod, B.L., Weaver, C.S., Wells, R.E., Rohay, A.C., Barnett, E.A., and
985 Knepprath, N.E., 2011, Connecting the Yakima fold and thrust belt to active faults in the
986 Puget Lowland, Washington: *Journal of Geophysical Research: Solid Earth*, v. 116, p. 1–
987 33, doi: 10.1029/2010JB008091.

988 Camp, V.E., 1981, Geologic studies of the Columbia Plateau: Part II. Upper Miocene basalt
989 distribution, reflecting source locations, tectonism, and drainage history in the Clearwater
990 embayment, Idaho.: *Geological Society of America Bulletin*, v. 92, p. 669–678, doi:
991 10.1130/0016-7606(1981)92<669:GSOTCP>2.0.CO;2.

992 Carroll, A.R., and Bohacs, K.M., 1999, Stratigraphic classification of ancient lakes: Balancing
993 tectonic and climatic controls: *Geology*, v. 27, p. 99–102, doi: 10.1130/0091-
994 7613(1999)027<0099:SCOALB>2.3.CO;2.

995 Casale, G., and Pratt, T.L., 2015, Thin- or thick-skinned faulting in the Yakima fold and thrust belt
996 (WA)? constraints from kinematic modeling of the Saddle Mountains anticline: *Bulletin of*
997 *the Seismological Society of America*, v. 105, p. 745–752, doi: 10.1785/0120140050.

998 Cheney, E.S., and Hayman, N.W., 2009, The Chiwaukum structural low: Cenozoic shortening of
999 the central Cascade Range, Washington State, USA: *Geological Society of America*
1000 *Bulletin*, v. 121, p. 1135-1153.

1001 Cheney, E.S., 2014, Tertiary stratigraphy and structure of the eastern flank of the Cascade Range,
1002 Washington: *Geological Society of America, Field Guides*, v. 38, p. 193–226, doi:
1003 10.1130/2014.0038(09).

1004 Cheng, H., Edwards, R.L., Shen, C.C., Polyak, V.J., Asmerom, Y., Woodhead, J., Hellstrom, J.,
1005 Wang, Y., Kong, X., Spötl, C. and Wang, X., 2013. Improvements in ²³⁰Th dating, ²³⁰
1006 Th and ²³⁴U half-life values, and U–Th isotopic measurements by multi-collector

1007 inductively coupled plasma mass spectrometry: *Earth and Planetary Science Letters*, v.
1008 371, p. 82-91.

1009 Choiniere, S., Swanson, D., 1979, Magnetostratigraphy and correlation of Miocene basalts of the
1010 northern Oregon Coast and Columbia Plateau Southeast Washington: *American Journal of*
1011 *Science*, v. 279, p. 755–777.

1012 Coe, R.S., Bogue, S., and Myers, C.W., 1978, Paleomagnetism of the Grande Ronde (lower
1013 Yakima) basalt exposed at Sentinel Gap: potential use for stratigraphic correlation:
1014 Rockwell Hanford Operations Report RHO-BWI-ST--2, 28 p.

1015 Czajkowski, J.L., Bowman, J.D., Schuster, J.E., and Wheeler, C.M., 2012, rev. 2015, Oil and gas
1016 wells in Washington State: Washington Division of Geology and Earth Resources Open
1017 File Report 2012-02, 1 Microsoft Excel file plus 4 p. text.

1018 Dahlstrom, C.D.A., 1969, Balanced cross sections: *Canadian Journal of Earth Sciences*, v. 6, p.
1019 743–757.

1020 Dickinson, W.R., and Gehrels, G.E., 2009, Use of U–Pb ages of detrital zircons to infer maximum
1021 depositional ages of strata: a test against a Colorado Plateau Mesozoic database: *Earth and*
1022 *Planetary Science Letters*, v. 288 (1), p. 115-125.

1023 Fiske, R.S., Hopson, C.A., and Waters, A.C., *Geology of Mount Rainier National Park*,
1024 Washington: U.S. Geological Survey Professional Paper 444, 93 p.

1025 Gehrels, G.E., 2000, Introduction to detrital zircon studies of Paleozoic and Triassic strata in
1026 western Nevada and northern California: *Geological Society of America Special Papers*, v.
1027 347, p. 1–17, doi: 10.1130/0-8137-2347-7.1.

1028 Geomatrix Consultants, 1996, Probabilistic Seismic Hazard Analysis DOE Hanford Site,
1029 Washington: Report WHC-SD-W236A-TI-002, Rev. 1, 372 p.:
1030 <http://pdw.hanford.gov/arpir/pdf.cfm?accession=D196005995>

1031 Gilmour, L.A., 2012, U/Pb ages of Eocene and younger rocks on the eastern flank of the central
1032 Cascade Range, Washington, USA [M.S. thesis]: Seattle, University of Washington, 50 p.

1033 Geslin, J.K., Link, P.K., Riesterer, J.W., Kuntz, M.A., and Fanning, C.M., 2002, Pliocene and
1034 Quaternary stratigraphic architecture and drainage systems of the Big Lost Trough,
1035 northeastern Snake River Plain, Idaho: Geological Society of America Special Paper, v.
1036 353, p. 11–26, doi: 10.1130/0-8137-2353-1.11.

1037 Gradstein, F.M., Ogg, J.G., Schmitz, M., and Ogg, G., 2012, Geomagnetic Polarity Time Scale, *in*
1038 The Geologic Time Scale 2012 2-Volume Set, Elsevier B.V., p. 85–113, doi:
1039 10.1016/B978-0-444-59425-9.00005-6.

1040 Hooper, P.R., Knowles, C.R., and Watkins, N.D., 1979, Magnetostratigraphy of the Imnaha and
1041 Grande Ronde Basalts in the southeastern part of the Columbia Plateau: American Journal
1042 of Science, v. 279, p. 737–754.

1043 Jenks, M.D., and Bonnicksen, B., 1989, Subaqueous basalt eruptions into Pliocene Lake Idaho,
1044 Snake River Plain, Idaho, in Chamberlain, V.E., Breckenridge, R.M., and Bonnicksen, B.,
1045 eds., Guidebook to the geology of northern and western Idaho and surrounding area: Idaho
1046 Geological Survey Bulletin 28, p. 17–34.

1047 Jutzeler, M., McPhie, J., and Allen, S.R., 2014, Facies architecture of a continental, below-wave-
1048 base volcanoclastic basin: The Ohanapecosh Formation, ancestral Cascades arc
1049 (Washington, USA): Bulletin of the Geological Society of America, v. 126, p. 352–376,
1050 doi: 10.1130/B30763.1.

1051 Keller, E.A., Gurrola, L., and Tierney, T.E., 1999, Geomorphic criteria to determine direction of
1052 lateral propagation of reverse faulting and folding: *Geology*, v. 27, p. 515–518, doi:
1053 10.1130/0091-7613(1999)027<0515:GCTDDO>2.3.CO;2.

1054 Lamb, A., 2015, Investigating Relationships Between the Yakima Fold and Thrust Belt and
1055 Basement Structure in Washington State Using Matched Filtering of Gravity and High-
1056 Resolution Aeromagnetic Data. In *AGU-SEG Workshop*, AGU.

1057 Lindsey, K.A., and Gaylord, D.R., 1990, Lithofacies and sedimentology of the Miocene-Pliocene
1058 Ringold Formation, Hanford site, south-central Washington: *Northwest Science*, v. 64, p.
1059 165–180.

1060 Lindsey, K.A., 1996, The Miocene to Pliocene Ringold Formation and Associated Deposits of the
1061 Ancestral Columbia River System, South-central Washington and North-central Oregon.:
1062 Washington Division of Geology and Earth Resources Open File Report 96-8, 176 p. text.

1063 Link, P.K., Fanning, C.M., and Beranek, L.P., 2005, Reliability and longitudinal change of detrital-
1064 zircon age spectra in the Snake River system, Idaho and Wyoming: An example of
1065 reproducing the bumpy barcode: *Sedimentary Geology*, v. 182, p. 101–142, doi:
1066 10.1016/j.sedgeo.2005.07.012.

1067 Ludwig, K.R., 2003, User's manual for Isoplot 3.00: a geochronological toolkit for Microsoft
1068 Excel, Berkeley Geochronology Center, University of California, Berkeley.

1069 Ludwig, K.R., 2012. Isoplot 3.75: A geochronology toolkit for Microsoft Excel. Berkeley
1070 Geochronology Berkeley Geochronology Center, University of California, Berkeley.

1071 Ludwig, K.R., Wallace, A.R. and Simmons, K.R., 1985, The Schwartzwalder uranium deposit; II,
1072 Age of uranium mineralization and lead isotope constraints on genesis: *Economic
1073 Geology*, v. 80, p. 1858-1871.

1074 Ludwig, K.R. and Paces, J.B., 2002, Uranium-series dating of pedogenic silica and carbonate,
1075 Crater Flat, Nevada: *Geochimica et Cosmochimica Acta*, v. 66, p. 487-506.

1076 Ludwig, K.R. and Titterton, D.M., 1994. Calculation of ^{230}ThU isochrons, ages, and
1077 errors. *Geochimica et Cosmochimica Acta*, 58(22), pp. 5031-5042.

1078 Malde, H.E., 1991, Quaternary geology and structural history of the Snake River Plain, Idaho and
1079 Oregon, in Morrison, R.B., ed., *Quaternary non-glacial geology, Conterminous U.S.:*
1080 *Boulder, Geological Society of America, The Geology of North America*, v. K-2, p. 251–
1081 280.

1082 Malone, S.D., Roth, G.H., and Smith, S.W., 1975, Details of microseismic earthquake swarms in
1083 the Columbia Basin, Washington: *Bulletin of the Seismological Society of America*, v. 65,
1084 p. 855–864.

1085 McCaffrey, R., Long, M.D., Goldfinger, C., Zwick, P.C., Nabelek, J.L., Johnson, C.K. and Smith,
1086 C., 2000, Rotation and plate locking at the southern Cascadia subduction zone:
1087 *Geophysical Research Letters*, v. 27, p. 3117–3120.

1088 McCaffrey, R., Qamar, A.I., King, R.W., Wells, R., Khazaradze, G., Williams, C.A., Stevens,
1089 C.W., Vollick, J.J. and Zwick, P.C., 2007, Fault locking, block rotation and crustal
1090 deformation in the Pacific Northwest: *Geophysical Journal International*, v. 169, p.1315-
1091 1340.

1092 McCaffrey, R., King, R.W., Payne, S.J., and Lancaster, M., 2013, Active tectonics of northwestern
1093 U.S. inferred from GPS-derived surface velocities: *Journal of Geophysical Research: Solid*
1094 *Earth*, v. 118, p. 709–723, doi: 10.1029/2012JB009473.

1095 McCaffrey, R., King, R.W., Wells, R.E., Lancaster, M., and Miller, M.M., 2016, Contemporary
1096 deformation in the Yakima fold and thrust belt estimated with GPS: *Geophysical Journal*
1097 *International*, p. 1–22, doi: 10.1093/gji/ggw252.

1098 McCalpin, J.P., and Nelson, A.R., 1996, Introduction to paleoseismology, *in* McCalpin, J.A. eds.,
1099 *Paleoseismology*: Academic Press, v. 95, p. 1-32.

1100 Middleton, L.T., Porter, M.L., and Kimmel, P.G., 1985, Depositional settings of the Chalk Hills
1101 and Glens Ferry Formations west of Bruneau, Idaho, in Flores, R.M., and Kaplan, S.S.,
1102 eds., *Cenozoic paleogeography of west-central United States*: Denver, Rocky Mountain
1103 Section, Society of Economic Paleontologists and Mineralogists, p. 37–54.

1104 Miller, R.B., Gordon, S.M., Bowring, S.A., Doran, B.A., McLean, N.M., Michels, Z.D., Shea,
1105 E.K., Whitney, D.L., Wintzer, N.E., and Mendoza, M.K., 2009, Linking deep and shallow
1106 crustal processes in an exhumed continental arc, North Cascades, Washington, in
1107 O’Connor, J.E., Dorsey, R.J., and Madin, I.P., eds., *Volcanoes to Vineyards: Geologic*
1108 *Field Trips through the Dynamic Landscape of the Pacific Northwest*: Geological Society
1109 of America Field Guide 15, p. 373–406, doi:10.1130/2009.fl d015(19).

1110 Miller, B.A., 2014, *On the origin of Umtanum Ridge: kinematics of Neogene slip* [M.S. Thesis]:
1111 Seattle, University of Washington, 47 p.

1112 Mitra, S., 1990, Fault-propagation folds: geometry, kinematic evolution, and hydrocarbon
1113 Traps: *AAPG Bulletin*, v. 74, p. 921–945.

1114 Morgan, J.K. and Morgan, N.H., 1995, A new species of *Capromeryx* (Mammalia: Artiodactyla)
1115 from the Taunton local fauna of Washington, and the correlation with other Blancan faunas
1116 of Washington and Idaho: *Journal of Vertebrate Paleontology*, v. 15, p. 160-170.

1117 Olsen, P.E., 1990, Tectonic, climatic, and biotic modulation of lacustrine ecosystems—examples
1118 from Newark Supergroup of eastern North America: Lacustrine basin exploration: Case
1119 studies and modern analogs: AAPG Memoir, v. 50, p. 209-224.

1120 Packer, D.R., and Johnston, J.M., 1979, Paleomagnetism and age dating of the Ringold Formation
1121 and loess deposits in the State of Washington: Oregon Geology, v. 41, p. 119–132.

1122 Petrus, J.A., and Kamber, B.S., 2012, VizualAge: A Novel Approach to Laser Ablation ICP-MS
1123 U-Pb Geochronology Data Reduction: Geostandards and Geoanalytical Research, v. 36, p.
1124 247– 270

1125 Pratt, T.L., 2012, Large-scale splay faults on a strike-slip fault system: The Yakima Folds,
1126 Washington State: Geochemistry, Geophysics, Geosystems, v. 13, p. 1–14, doi:
1127 10.1029/2012GC004405.

1128 Press, W.H., Flannery, B.P., Teukolsky, S.A., and Vetterling, W.T., 1986, Numerical recipes: *in*
1129 The Art of Scientific Computing, Cambridge Univ. Press, Cambridge, 186 p.

1130 Price, E. H., and Watkinson, A.J., 1989, Structural geometry and strain distribution within eastern
1131 Umtanum fold ridge, south–central Washington: *in* Volcanism and Tectonism in the
1132 Columbia River Flood-Basalt Province, Geological Society of America Special Paper, S. P.
1133 Reidel and P. R. Hooper (Editors), v. 239, p. 265–281.

1134 Reidel, S. P., and Fecht, K.R., Wanapum and Saddle Mountains Basalts of the Cold Creek
1135 Syncline area, Surface Geology of the Cold Creek Syncline. Rockwell Hanford Operations
1136 Report RHO-BWI-ST--14, 45 p.

1137 Reidel, S.P., 1983, Stratigraphy and petrogenesis of the Grande Ronde Basalt from the deep
1138 canyon country of Washington, Oregon, and Idaho: Bulletin of the Geological Society of
1139 America, v. 94, p. 519–542, doi: 10.1130/0016-7606(1983)94<519:SAPOTG>2.0.CO;2.

1140 Reidel, S.P., 1984, The Saddle Mountains: the evolution of an anticline in the Yakima fold belt:
1141 American Journal of Science, v. 284, p. 942–978.

1142 Reidel, S.P., Scott, G.R., Bazard, D.R., Cross, R.W., and Dick, B., 1984, Post-12 Million Year
1143 Clockwise Rotation in the central Columbia Plateau, Washington: Tectonics, v. 3, p. 251-
1144 273, doi: 10.1029/TC003i002p00251.

1145 Reidel, S.P., 1988, Geologic Map of the Saddle Mountains, South-Central Washington:
1146 Washington Division of Geology and Earth Resources Map GM-38, scale 1:48 000, 5
1147 sheets.

1148 Reidel, S.P., Fecht, K.R., Hagood, M.C., and Tolan, T.L., 1989a, The geologic evolution of the
1149 central Columbia Plateau: Geological Society of America Special Papers, v. 239, p. 247-
1150 264, doi: 10.1130/SPE239-p247.

1151 Reidel, S.P., Tolan, T.L., Hooper, P.R., Beeson, M.H., Fecht, K.R., Bentley, R.D., and Anderson,
1152 J.L., 1989b, The Grande Ronde Basalt, Columbia River Basalt Group; Stratigraphic
1153 descriptions and correlations in Washington, Oregon, and Idaho: Geological Society of
1154 America Special Papers, v. 239, p. 21–54, doi: 10.1130/SPE239-p21.

1155 Reidel, S.P., Campbell, N.P., Fecht, K.R., and Lindsey, K.A., 1994, Late Cenozoic Structure and
1156 Stratigraphy of South-Central Washington: Regional Geology of Washington State, Bull.
1157 80, p. 159–180.

1158 Reidel, S.P., Camp, V.E., Tolan, T.L., Kauffman, J.D., and Garwood, D.L., 2013, Tectonic
1159 evolution of the Columbia River flood basalt province: Special Paper of the Geological
1160 Society of America, v. 497, p. 293–324, doi: 10.1130/2013.2497(12).

- 1161 Reppenning, C.A., 1987, Biochronology of the microtine rodents of the United States: *in* M.O.
1162 Woodburne, ed., *Cenozoic Mammals of North America: Geochronology and*
1163 *Biostratigraphy*. University of California Press, Berkeley, p. 236-268.
- 1164 Rowan, M.G., and Linares, R., 2000, Fold-evolution matrices and axial-surface analysis of fault
1165 bend folds: Application to the Medina anticline, Eastern Cordillera, Colombia: *AAPG*
1166 *Bulletin*, v. 84, p. 741–764.
- 1167 Rudnick, R.L., and Gao, S., 2003, Composition of the continental crust, *in* Holland H.D., and
1168 Turekian, K.K., eds., *Treatise on Geochemistry*: San Diego, California, Elsevier, p. 1-64.
- 1169 Sadler, J.L., and Link, P.K., 1996, The Tuana Gravel: Early Pleistocene response to longitudinal
1170 drainage of a late-stage rift basin, western Snake River Plain, Idaho: *Northwest Geology*, v.
1171 26, p. 46–62.
- 1172 Saltus, R.W., 1993, Upper-crustal structure beneath the Columbia River Basalt Group,
1173 Washington: Gravity interpretation controlled by borehole and seismic studies: *Geological*
1174 *Society of America Bulletin*, v. 105, p. 1247–1259.
- 1175 Saylor, J.E. and Sundell, K.E., 2016, Quantifying comparison of large detrital geochronology data
1176 sets: *Geosphere*, p. GES01237-1.
- 1177 Schmitz, M.D., and Bowring, S.A., 2001, U-Pb zircon and titanite systematics of the Fish Canyon
1178 Tuff: An assessment of high-precision U-Pb geochronology and its application to young
1179 volcanic rocks: *Geochimica et Cosmochimica Acta*, v. 65, p. 2571–2587, doi:
1180 10.1016/S0016-7037(01)00616-0.
- 1181 Shaw, D.M., Dostal, Jaroslav, and Keays, R.R., 1976, Additional estimates of continental surface
1182 Precambrian shield composition in Canada: *Geochimica et Cosmochimica Acta*, v. 40, p.
1183 70-83.

- 1184 Sláma, J., Košler, J., Condon, D.J., Crowley, J.L., Gerdes, A., Hanchar, J.M., Horstwood, M.S.,
1185 Morris, G.A., Nasdala, L., Norberg, N. and Schaltegger, U., 2008, Plešovice zircon—a new
1186 natural reference material for U–Pb and Hf isotopic microanalysis: *Chemical Geology*, v.
1187 249, p. 1-35.
- 1188 Smith, G.A., 1988, Neogene synvolcanic and syntectonic sedimentation in central Washington:
1189 *Geological Society of America Bulletin*, v. 100, p. 1479–1492, doi: 10.1130/0016-
1190 7606(1988)100<1479.
- 1191 Smith, G.A., 1993, Missoula flood dynamics and magnitudes inferred from sedimentology of
1192 slack-water deposits on the Columbia Plateau, Washington: *Geological Society of America*
1193 *Bulletin*, v. 105, p. 77–100, doi: 10.1130/0016-7606(1993)105<0077:MFDAMI>2.3.CO;2.
- 1194 Smith, G.R., Morgan, N., and Gustafson, E., 2000, Fishes of the Mio-Pliocene Ringold Formation,
1195 Washington: Pliocene Capture of the Snake River by the Columbia River, *Papers*
1196 *University of Michigan Museum of Paleontology*, v. 32, p. 1–47.
- 1197 Staisch, L.M., Bennett, S.E.K., Sherrod, B.L., and Kelsey, K.M., 2015, Holocene to Neogene
1198 tectonics in central Washington: assessing seismic hazards from the geomorphic, geologic,
1199 and paleoseismic record of the Yakima Folds: Abstract T31B-2892 presented at 2015 Fall
1200 Meeting, AGU, San Francisco, California 12-16 December.
- 1201 Staisch, L.M., 2016, Miocene to Quaternary deformation history of the Yakima fold province as
1202 determined from geomorphic and geologic records: implications for seismic hazard in
1203 central Washington: Abstract T9-276106 presented at 2016 Geological Society of America,
1204 Rocky Mountain Section Meeting, 18-19 May.

1205 Steiger, R. H., and E. Jager, 1977, Subcommittee on geochronology: Convention on use of decay
1206 constants in geochronology and cosmochronology: *Earth Planet. Sci. Lett.*, v. **36**, p. 359–
1207 362, doi:10.1016/0012-821X(77)90060-7.

1208 Suppe, J. and Medwedeff, D.A., 1990. Geometry and kinematics of fault-propagation folding:
1209 *Ecolgae Geologicae Helvetiae*, v. 83, p. 409-454.

1210 Suppe, J., Chou, G.T., and Hook, S.C., 1992, Rates of folding and faulting determined from growth
1211 strata, *in* McClay, K.R., eds., *Thrust Tectonics*: Chapman and Hall, London, p. 104–122.

1212 Suppe, J., 1985, *Principles of Structural Geology*: Prentice-Hall, Englewood Cliffs, N.J., 537 p.

1213 Swanson, D.A., Wright, T.L., Hooper, P.R., and Bentley, R.D., 1979, Revisions in Stratigraphic
1214 Nomenclature of the Columbia River Basalt Group: U.S. Geological Survey Bulletin 1457-
1215 G, 59 p.

1216 Tabor, R.W., Frizzell, V.A., Vance, J.A., and Naeser, C.W., 1984, Ages and stratigraphy of lower
1217 and middle Tertiary sedimentary and volcanic rocks of the central Cascades, Washington:
1218 application to the tectonic history of the Straight Creek fault (USA).: *Geological Society of*
1219 *America Bulletin*, v. 95, p. 26–44, doi: 10.1130/0016-
1220 7606(1984)95<26:AASOLA>2.0.CO;2.

1221 Tabor, R.W., Frizzell Jr., V.A., Booth, D.B., and Waitt, R.B., 2000, Geologic map of the
1222 Snoqualmie Pass 30' x 60' quadrangle, Washington, U.S. Geological Survey Scientific
1223 Investigations Map I-2538, scale 1:100,000.

1224 Taylor S.R., and McLennan S.M., 1985, *The Continental Crust—Its Composition and Evolution*:
1225 Palo Alto, California, Blackwell Scientific Publishers, 312 p.

- 1226 Telford, W.M., Geldart, L.P., and Sheriff, R.E., 1990, Electrical Properties of Rocks and Minerals,
1227 *in* Telford, W.M., eds., Applied geophysics (Vol. 1), Cambridge University Press, p. 283-
1228 292.
- 1229 Tolan, T.L., Martin, B.S., Reidel, S.P., Anderson, J.L., Kindsey, K.A., and Burt, W., 2009, An
1230 introduction to the stratigraphy, structural geology, and hydrogeology of the Columbia
1231 River flood basalt province: A primer for the GSA Columbia River Basalt Group field
1232 trips, *in* O'Connor, J.E., Dorsey, R.J., and Madin, I.P., eds., Volcanoes to Vineyards—
1233 Geologic Field Trips through the Dynamic Landscape of the Pacific Northwest: Geological
1234 Society of America Field Guide 15, p. 599–645.
- 1235 Watanabe, Y. and Nakai, S.I., 2006, U-Th radioactive disequilibrium analyses for JCp-1, coral
1236 reference distributed by the Geological Survey of Japan: *Geochemical Journal*, v. 40, p.
1237 537-541.
- 1238 Watters, T.R., 1989, Periodically spaced anticlines of the Columbia plateau: *in* S.P. Reidel and
1239 P.R. Hooper, eds., *Volcanism and Tectonism in the Columbia River Flood-Basalt Province*,
1240 Geological Society of America Special Paper, v. 239, p. 283–292.
- 1241 Wells, D.L. and Coppersmith, K.J., 1994, New empirical relationships among magnitude, rupture
1242 length, rupture width, rupture area, and surface displacement: *Bulletin of the seismological*
1243 *Society of America*, v. 84, p. 974-1002.
- 1244 Wells, R.E., and McCaffrey, R., 2013, Steady rotation of the Cascade arc: *Geology*, v. 41, p. 1027–
1245 1030, doi: 10.1130/G34514.1.
- 1246 Wells, R.E., Simpson, R.W., Bentley, R.D., Beeson, M.H., Mangan, M.T., and Wright, T.L., 1989,
1247 Correlation of Miocene flows of the Columbia River Basalt Group from the central

1248 Columbia River Plateau to the coast of Oregon and Washington: Volcanism and Tectonism
1249 in the Columbia River Flood-Basalt Province, doi: 10.1130/SPE239-p113.

1250 Wells, R.E., 1998, Fore-arc migration in Cascadia and its neotectonic significance: *Geology*, v. 26,
1251 p. 759–762, doi: 10.1130/0091-7613(1998)026<0759:FAMICA>2.3.CO;2.

1252 West, M.W., Ashland, F.X., Busacca, A.J., Berger, G.W., and Shaffer, M.E., 1996, Late
1253 Quaternary deformation, Saddle Mountains anticline, south-central Washington: *Geology*,
1254 v. 24, p. 1123–1126, doi: 10.1130/0091-7613(1996)024<1123:LQDSMA>2.3.CO;2.

1255 Wilkerson, S.M., Apotria, T., and Farid, T., 2002, Interpreting the geologic map expression of
1256 contractional fault-related fold terminations: Lateral/oblique ramps versus displacement
1257 gradients: *Journal of Structural Geology*, v. 24, p. 593–607.

1258 Wilson, M.S., Dyman, T.S., and Condon, S.M., 2008, Evaluation of Well-Test Results and the
1259 Potential for Basin-Central Gas in the Columbia Basin, Central Washington: *in* *Geologic*
1260 *Assessment of Undiscovered Gas Resources of the Eastern Oregon and Washington*
1261 *Province U.S. Geological Survey Digital Data Series 69-O, CD-ROM.*

1262

1263 **FIGURES**

1264 **Figure 1.**

1265 Regional map of the Yakima Fold Province with inset of the tectonic setting in the western U.S. for
1266 reference. Abbreviations on inset include PP (Pacific Plate), NAP (North American Plate), EP
1267 (Explorer Plate), GP (Gorda Plate), JDFP (Juan de Fuca Plate), and SAFZ (San Andreas Fault
1268 Zone). Abbreviations on map include MR (Manastash Ridge), UR (Umtanum Ridge), YR (Yakima
1269 Ridge), AR (Ahtanum Ridge), TR (Toppenish Ridge), FH (Frenchman Hills), RH (Rattlesnake
1270 Hills), HHH (Horse Heaven Hills), BM (Boyleston Mountains), SG (Sentinel Gap), and YC

1271 (Yakima Canyon). Digital elevation model (DEM) and hillshade derivative is 10-meter resolution
1272 U.S. Geological Survey national map database (ned.usgs.gov). Active fault locations are from the
1273 U.S. Geological Survey Quaternary Fault database (earthquake.usgs.gov/hazards/qfaults).
1274 Earthquake locations and magnitudes are from the ANSS earthquake catalog
1275 (<http://www.quake.geo.berkeley.edu/anss/catalog-search.html>). Borehole site locations are from
1276 Czajkowski et al. (2012). Strain boundary locations are from McCaffrey et al. (2016). The location
1277 of Figure 2 is indicated by a thick black outline.

1278 **Figure 2.**

1279 Geologic map of the Saddle Mountains. Geology was digitized and modified from Reidel (1988).
1280 The location of fault traces and fold axes are based on original mapping from Reidel (1988), field
1281 observations, cross section results, and/or aeromagnetic anomalies (Fig. 12). Structural
1282 measurements include new bedding orientations from this work and published orientations from
1283 Reidel (1988). Paleoseismic trench locations from West et al. (1996) are indicated by red boxes.
1284 The majority of the background hillshade is of 2-meter resolution LiDAR data from the Puget
1285 Sound LiDAR Consortium (pugetsoundlidar.ess.washington.edu/lidardata/), and the remainder is
1286 10-meter data from the national map database (ned.usgs.gov). Borehole site locations are from
1287 Czajkowski et al. (2012). Stratigraphic sections of the Ringold Formation are shown in Figure 5.
1288 Cross sections along transects A-A' and B-B' are shown in Figure 13. Acronyms used include:
1289 SMF (Saddle Mountains fault), SMA (Saddle Mountains anticline), SMS (Saddle Mountains
1290 syncline), CA (Crest anticline), and SF (Smyrna fault).

1291 **Figure 3.**

1292 Generalized stratigraphy of the Saddle Mountains, based on exploratory borehole measurements
1293 (Fig. A1) and previous work on the relative ages of geologic units in the Cascadian backarc (Fiske,

1294 1963; Bentley, 1977; Packer and Johnson, 1979; Swanson et al., 1979; Camp, 1981; Reidel and
1295 Fecht, 1981; 1987; Tabor et al., 1984; Repenning, 1987; Reidel, 1988; Smith et al., 1988; Morgan
1296 and Morgan, 1995; Tabor et al., 2000; Miller et al., 2009; Tolan et al., 2009; Gilmour, 2012; Barry
1297 et al., 2013; Reidel et al., 2013; Cheney, 2014; Jutzeler et al., 2014; this work). Faded regions
1298 indicate time periods during which the depositional age of a unit is disputed, with dashed lines as
1299 alternative depositional cessations. “Shazam” lines indicate possible coeval deposition of
1300 temporally overlapping units.

1301 **Figure 4.**

1302 Photograph and photo interpretation of an exposure of the Saddle Mountains fault (SMF) near the
1303 Mathews Canyon section. The lower Ringold strata exhibit beds inclined to the south, whereas the
1304 upper lacustrine Ringold strata are sub-horizontal. Here, the SMF places Grande Ronde N2
1305 Columbia River Basalt Group (CRBG) strata, locally overturned, on top of the Ringold Formation.
1306 Photo by L. Staisch.

1307 **Figure 5.**

1308 Stratigraphic columns measured in the Ringold Formation near the Saddle Mountains.
1309 Stratigraphic sections are organized from west (left) to east (right) and are hung on the common
1310 marker bed horizon identified in 5 out of 6 sections. The base of each stratigraphic column is on
1311 the top of the Elephant Mountain Member (meter 0). Samples collected from strata are located to
1312 the right of each stratigraphic column and are identified by sample type (symbol) and ID number.

1313 **Figure 6.**

1314 Field photos of the Ringold Formation near the Saddle Mountains anticline. (A) Photo of footwall
1315 conglomeratic section with Harvey Kelsey for scale, taken near the Schoolhouse section (Fig. 5).
1316 (B) Steeply dipping petrocalcic horizon near the Jericho section (Fig. 5) with Jura Staisch for scale.

1317 (C) Photo of hanging wall debris flow and paleosols horizons with Harvey Kelsey for scale, taken
1318 near Feedlot section (Fig. 5). (D) Calcified rhyoliths from paleosols horizon in Schoolhouse
1319 section. (E) Petrocalcite horizon developed directly on Elephant Mountain Member, Harvey
1320 Kelsey for scale. (F) Calcic cement developed in mudflow strata of the Jericho section, rock
1321 hammer for scale. Photos by L. Staisch.

1322 **Figure 7.**

1323 Topographic map of the eastern portion of the Saddle Mountains anticline with a 50-meter contour
1324 interval. The base of the upper Ringold strata, at elevation 290, is identified by a thick black line.
1325 This correlates to the elevation of the Taunton Ringold section, which was
1326 magnetostratigraphically dated by Packer and Johnson (1979) at 3.596–6.033 Ma.

1327 **Figure 8.**

1328 Photograph and photo interpretation of a NW-trending, NE-vergent anticline in the hanging wall of
1329 the SMF. Fold deforms the CRBG strata as well as the Ringold strata and caliche (Fig. 6B). Photo
1330 by L. Staisch.

1331 **Figure 9.**

1332 Concordia plots showing the U-Pb zircon age results for tephra interbedded within the Ringold
1333 Formation. On all plots, solid gray ellipses are the concordant and coherent group of zircons used
1334 to calculate the concordia age. Dashed ellipses are dated zircons that are not concordant, have high
1335 analytical errors, or are otherwise considered outliers. The thick black ellipse in each plot is the
1336 calculated concordia age. On each plot, we report the concordia age and 2σ uncertainty, mean
1337 square of the weighted deviates (MSWD), and the number of zircons (N) within the coherent
1338 group. (A) Results for sample 15SM002 from the hanging wall (lowermost sample from directly
1339 above the weathered basalt in the Jericho section). (B) Results from 16SM001, upper sample from

1340 near the top of the Jericho section (C) Results from 15SM006, stratigraphically the lowest sample
1341 collected from the footwall (Schoolhouse section). (D) Results from 15SM007, the second lowest
1342 sample collected from the footwall (Schoolhouse section). (E) Results from 15SM003, collected
1343 just below the channel fill marker bed in the footwall (Mathews Canyon section). (F) Result from
1344 15SM004, reworked tephra collected near the top of the footwall strata (Mathews Canyon section).

1345 **Figure 10.**

1346 Geomorphic map of the Columbia Basin (CB) and Snake River Plain (SRP). Major rivers are
1347 shown in black and labeled. The mapped locations of the Atlanta lobe of the Idaho Batholith and
1348 the Challis Volcanic Group are shown in patterned shades of grey (Bond et al., 1978; Johnson and
1349 Raines, 1996). Sites where detrital zircon samples have been analyzed are indicated by light grey
1350 for modern river samples, black for Pleistocene aged deposits, medium-light grey for Pliocene
1351 strata, and medium dark grey for Miocene strata. In the legend, the references for each sample
1352 source are indicated by * for Greslin et al. (1999, 2002), † for Link et al. (2005), and ‡ for Beranek
1353 et al. (2006). Values of statistical comparison (similarity, likeness, and K-S test) between Saddle
1354 Mountains and Snake River Plain detrital samples are available in Table A9. DEM and derivative
1355 hillshade are from 90-meter data (<http://srtm.csi.cgiar.org/>).

1356 **Figure 11.**

1357 U-Series age results for aliquots of petrocalcic horizons. All ages reported are for individual
1358 aliquots with 2σ analytical uncertainty. Aliquots with excess Thorium do not provide an
1359 interpretable age due to detrital ^{230}Th contamination or diagenetic depletion of Uranium. (A)
1360 Results for sample 15SM011, aliquots A-C, collected from the upper caliche horizon in footwall
1361 Schoolhouse section. (B) Results for sample 16SM002, aliquots A1-A2, B1-B3, C1-C2, D1, E1-
1362 E2, and F1-F2 collected from the thick upper calcrete in the hanging wall Jericho section. (C)

1363 Results from sample 16SM003, aliquots A1-A3, B1-B3, C1, D1-D3, and G1-G2 collected from the
1364 same location as 16SM002. (D) Results for all samples plotted on an isochron age plot. Data points
1365 with white interiors are aliquots that did not produce an interpretable age or uncertainty. The inset
1366 shows the weighted mean age derived for sample 15SM011.

1367 **Figure 12.**

1368 Map of 100-m resolution total field magnetic anomaly data measured over the Saddle Mountains
1369 anticline. More positive magnetic anomalies are shown in warm colors, and negative anomalies are
1370 shown in cool colors. Basic structures and cross section transects A-A' and B-B' are plotted for
1371 reference. Fault traces are from Figure 2, and were modified from Reidel (1988) based on new
1372 field observations, cross section results, and strong horizontal gradients from the magnetic anomaly
1373 data. The main differences in fault trace location are to the west of Smyrna bench, where the fault
1374 trace is obscured by alluvial fans (Fig. 2).

1375 **Figure 13.**

1376 Line-balanced cross sections and magnetic anomaly data and modeling along transects A-A' (upper
1377 plots) and B-B' (lower plots). For each transect, the observed magnetic anomaly data is extracted
1378 (cyan line) and modeled based on magnetic parameters and cross section construction (dark blue
1379 line). The cross sections that produce the best-fit modeled anomaly data are displayed in the lower
1380 panels to a depth of 8 km. Elevation data, surface geology, and bedding orientations are extracted
1381 from DEMs and geologic mapping and projected along the cross section transects. The total
1382 shortening estimated is 1.3 and 1.0 km for A-A' and B-B', respectively.

1383 **Figure 14.**

1384 Comparison of cross sections A-A' and B-B'. The upper diagram shows the cross sections overlain
1385 over each other, where the SMF and topography along A-A' and B-B' are depicted in white and

1386 black, respectively. The lower diagram shows a schematic oblique block diagram of a lateral ramp
1387 accommodating along-strike variation in the SMF. In this model, the lateral ramp would
1388 accommodate a component right lateral motion.

1389 **Figure 15.**

1390 The sediment accumulation rate of the Ringold formation in the footwall of the Saddle Mountains
1391 Fault is estimated using a linear regression of U-Pb zircon tephra ages and stratigraphic position of
1392 tephra. The age of the marker bed horizon is estimated using this sediment accumulation rate at 6.8
1393 ± 0.35 Ma.

1394 **Figure 16.**

1395 Schematic depiction of temporal variation in tectonically-generated uplift along the Saddle
1396 Mountains anticline. Relief estimates in deep time are made from the differences in the
1397 stratigraphic height growth strata deposited on the SMF footwall (T_F) and on the hanging wall
1398 (T_H). (A) After emplacement of the 10–10.5 Ma Elephant Mountain Member, anticlinal growth
1399 generated relief along the Saddle Mountains. By the time the channel fill marker bed was deposited
1400 (6.8 Ma), between 23 and 28 meters of relief had been generated. (B) Since 6.8 Ma, 187 meters of
1401 uplift were accommodated along the eastern portion of the SMA and 287 meters of uplift were
1402 accommodated along the western portion of the SMA. After 6.8 Ma, footwall strata are dominated
1403 by lacustrine facies and paleosols formation. Upper Ringold deposition continued until ~ 3.5 Ma. In
1404 the hanging wall, lacustrine strata are absent, but loess accumulation and paleosols formation
1405 continued.

1406 **Figure 17.**

1407 Estimates of the time required to accumulate sufficient strain energy along the Saddle Mountains
1408 fault for earthquakes of a given magnitude. (A) Linear plot of the strain accumulation interval in

1409 light gray is calculated from the paleoseismically-derived slip rate estimate (West et al., 1996) and
1410 the interval in patterned dark gray is calculated from our geologically derived latest-Miocene to
1411 present slip rate. (B) A log-linear plot of the same results as (A) to emphasize the short time
1412 interval required to accumulate strain energy for M5–M6.5.

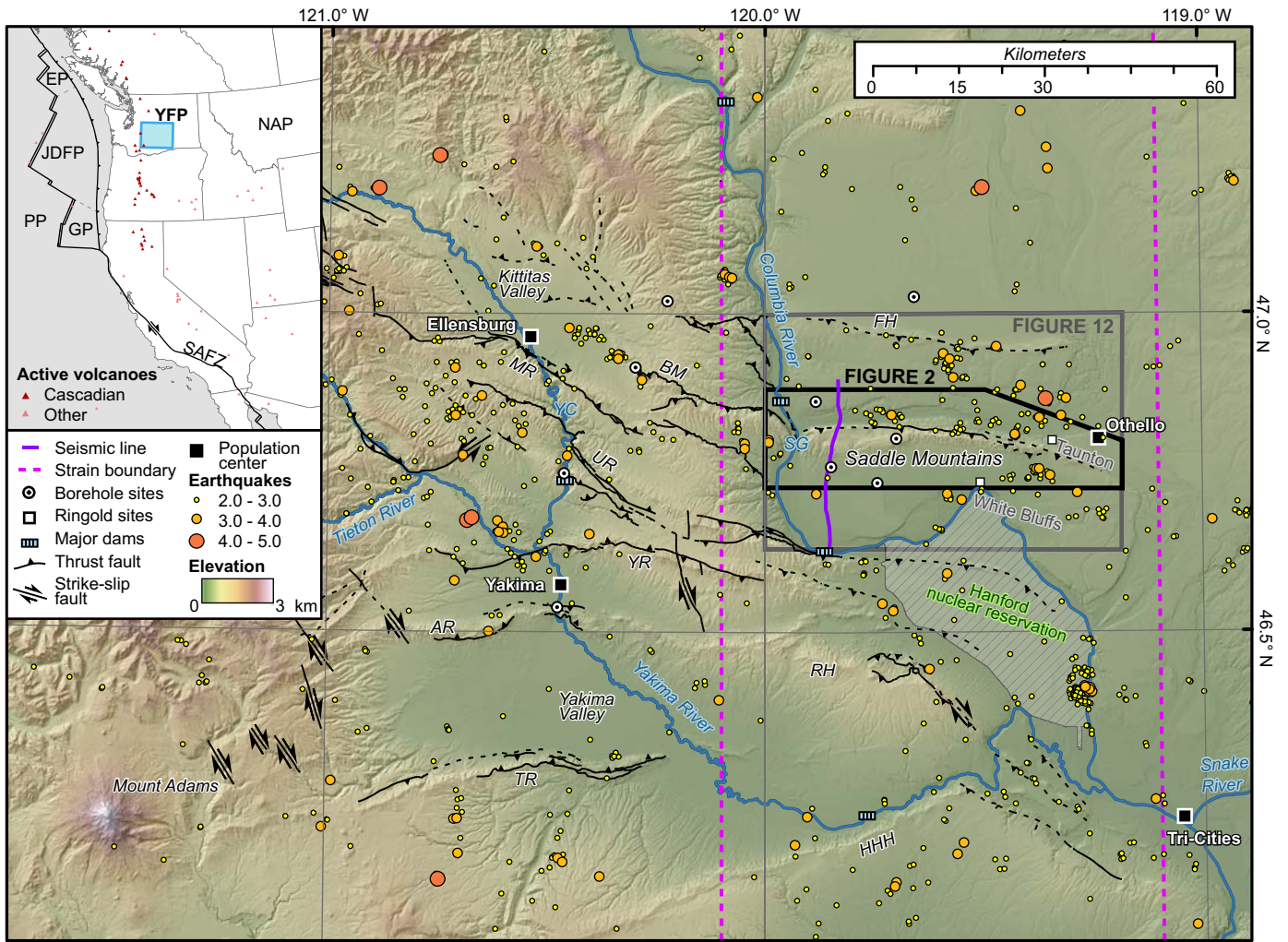


Figure 1

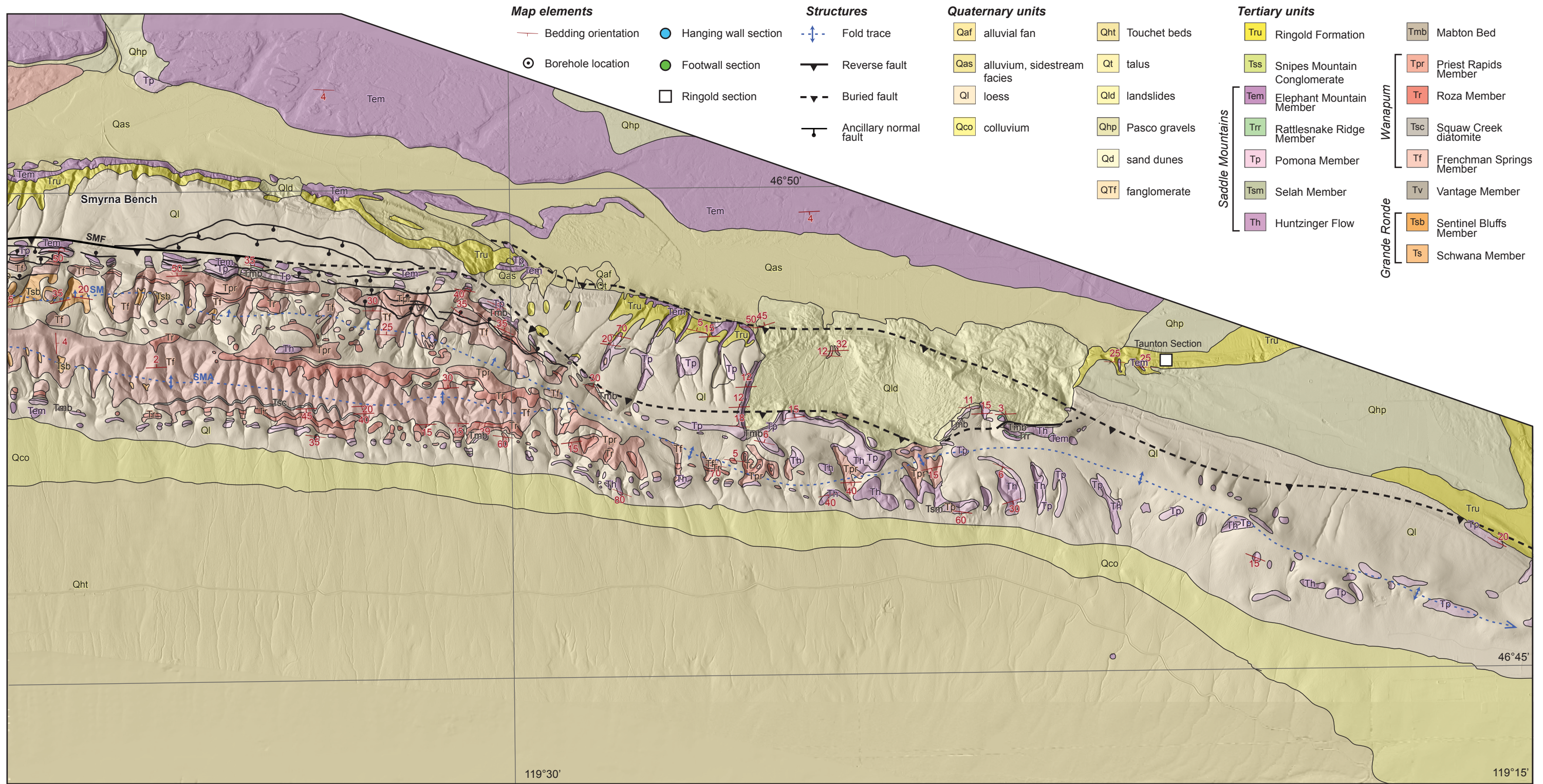
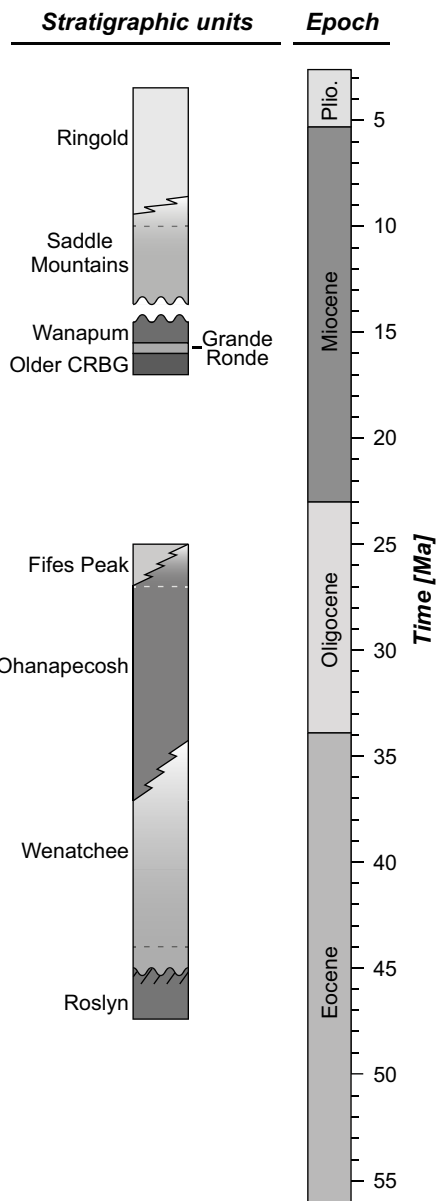
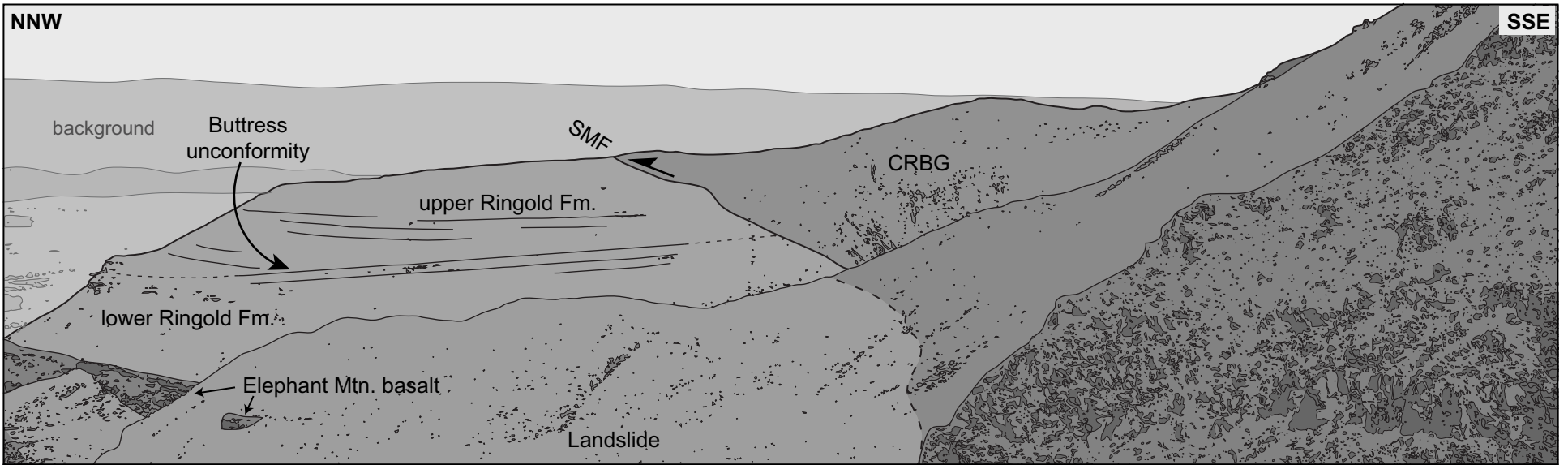
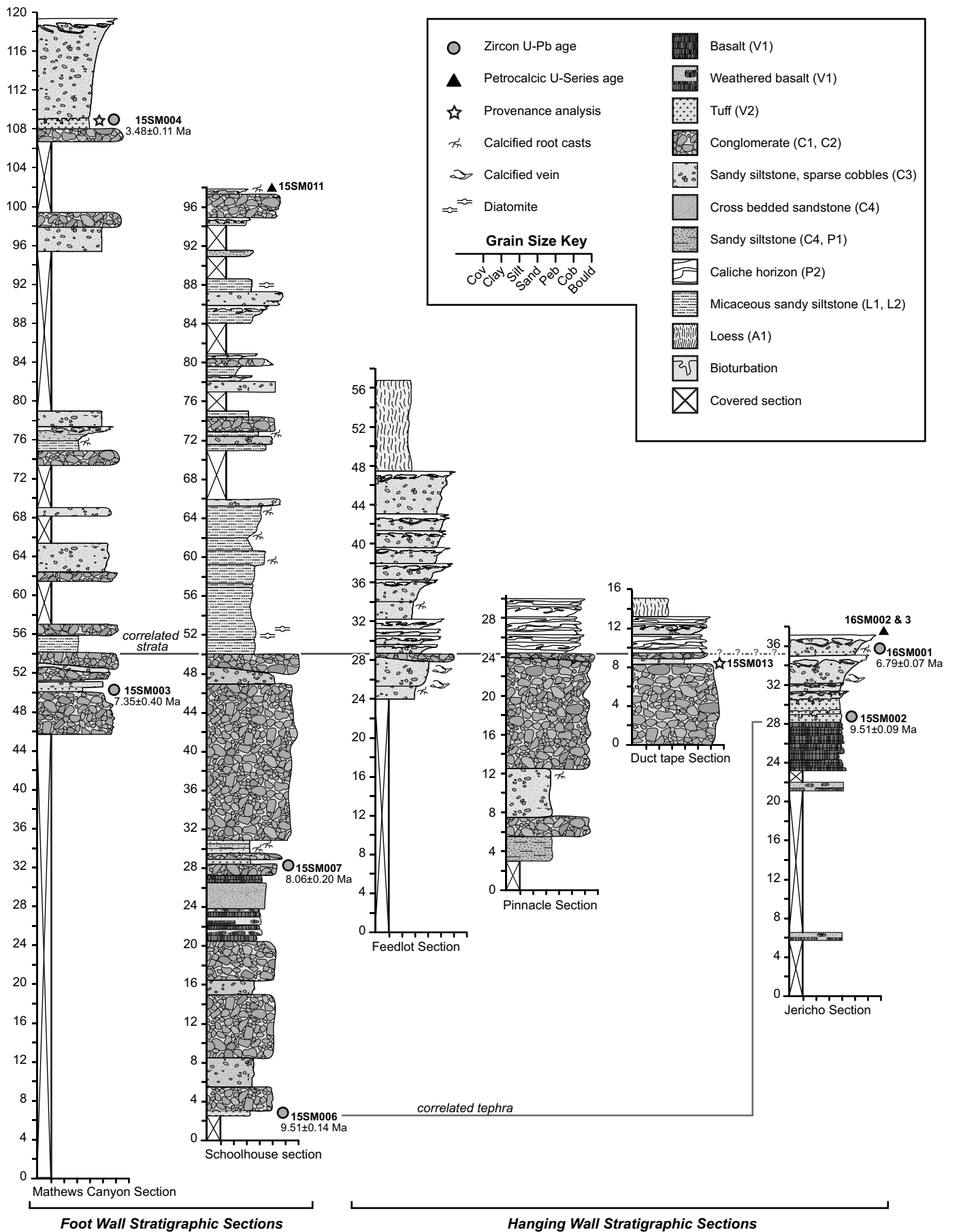


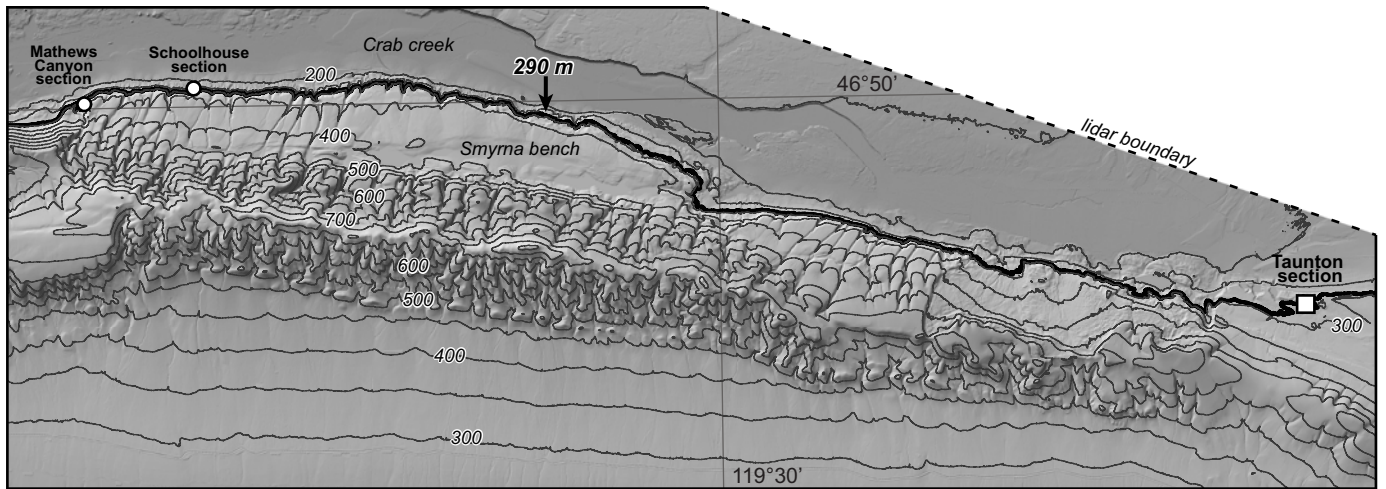
Figure 2b

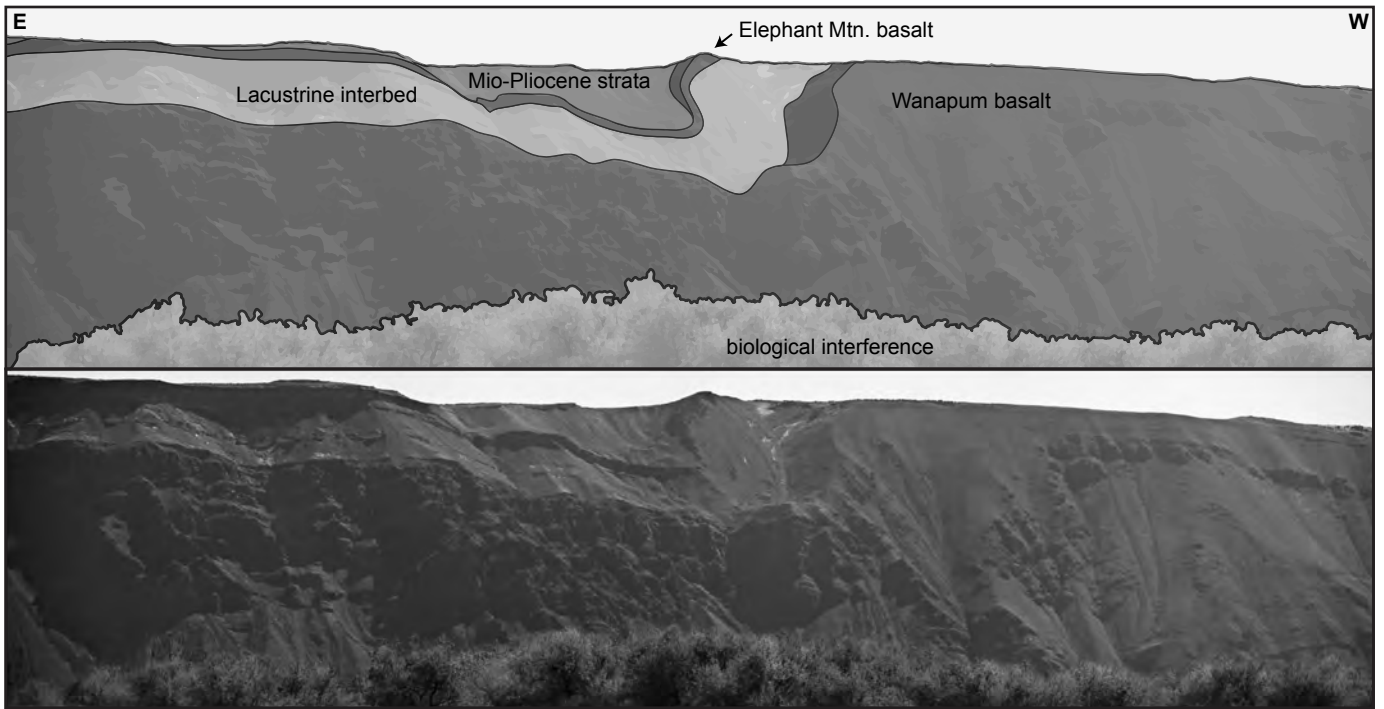


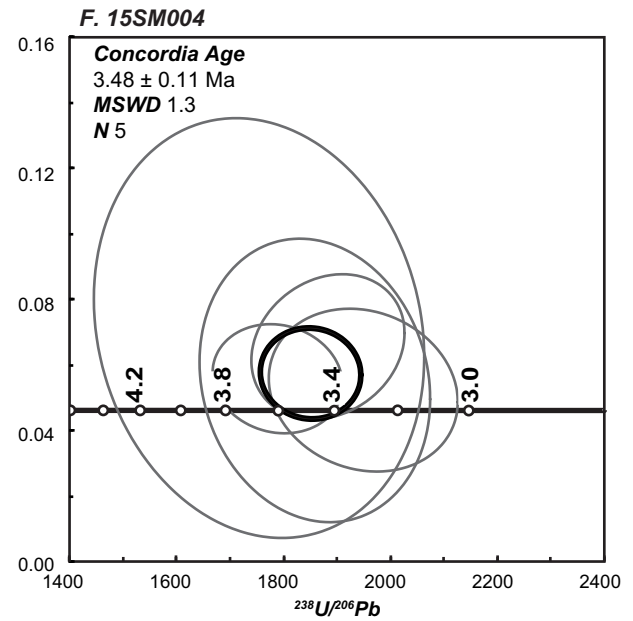
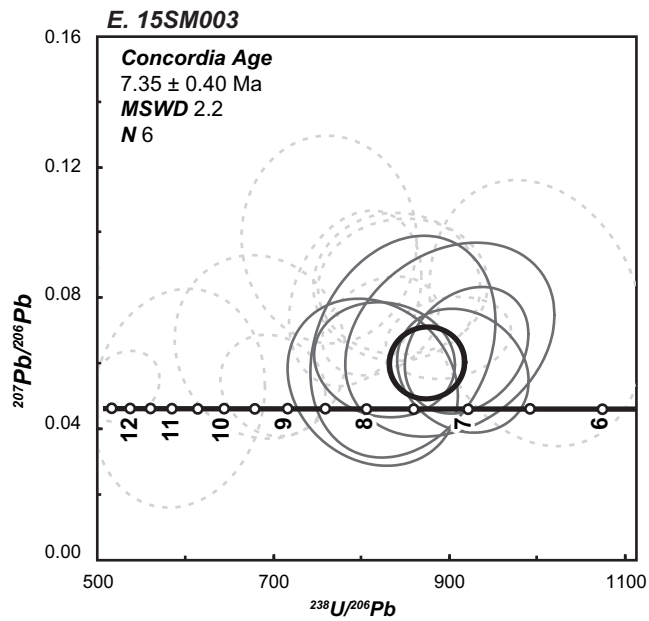
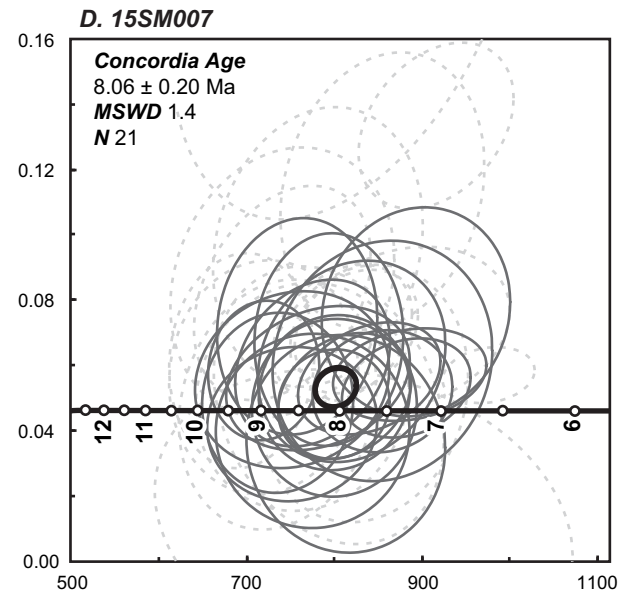
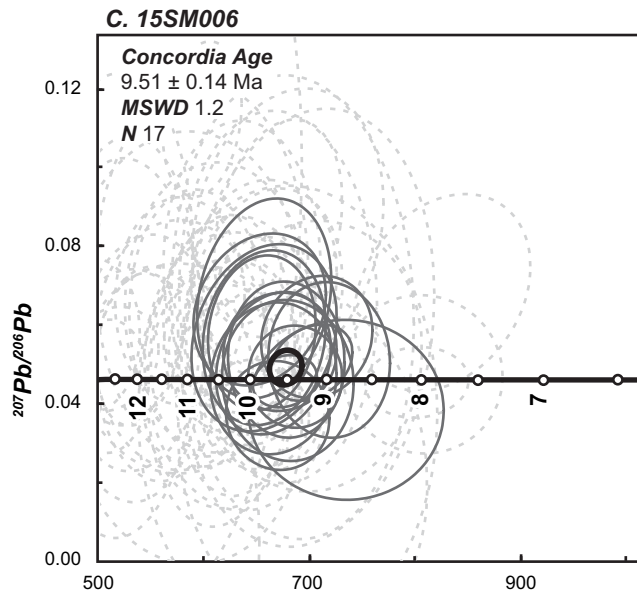
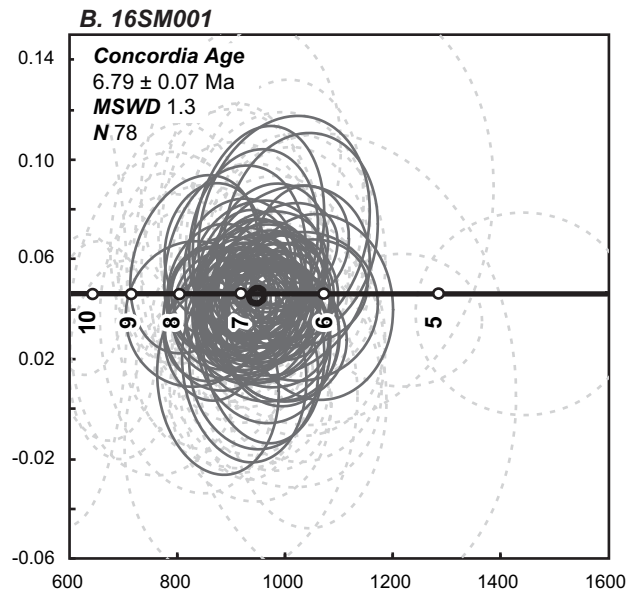
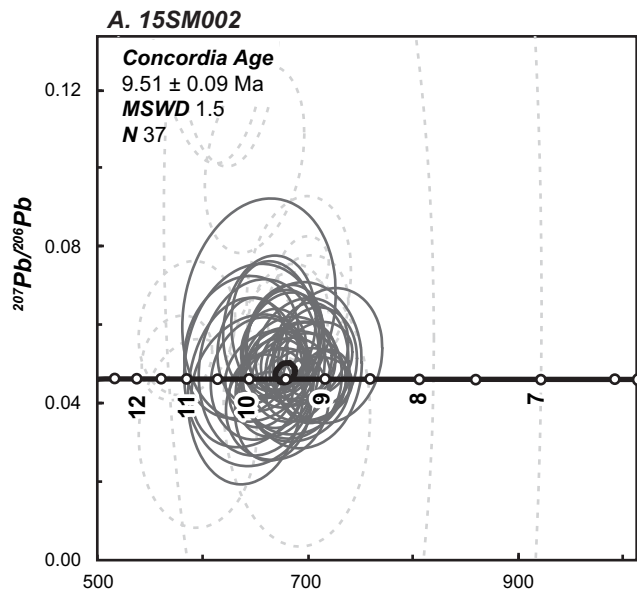


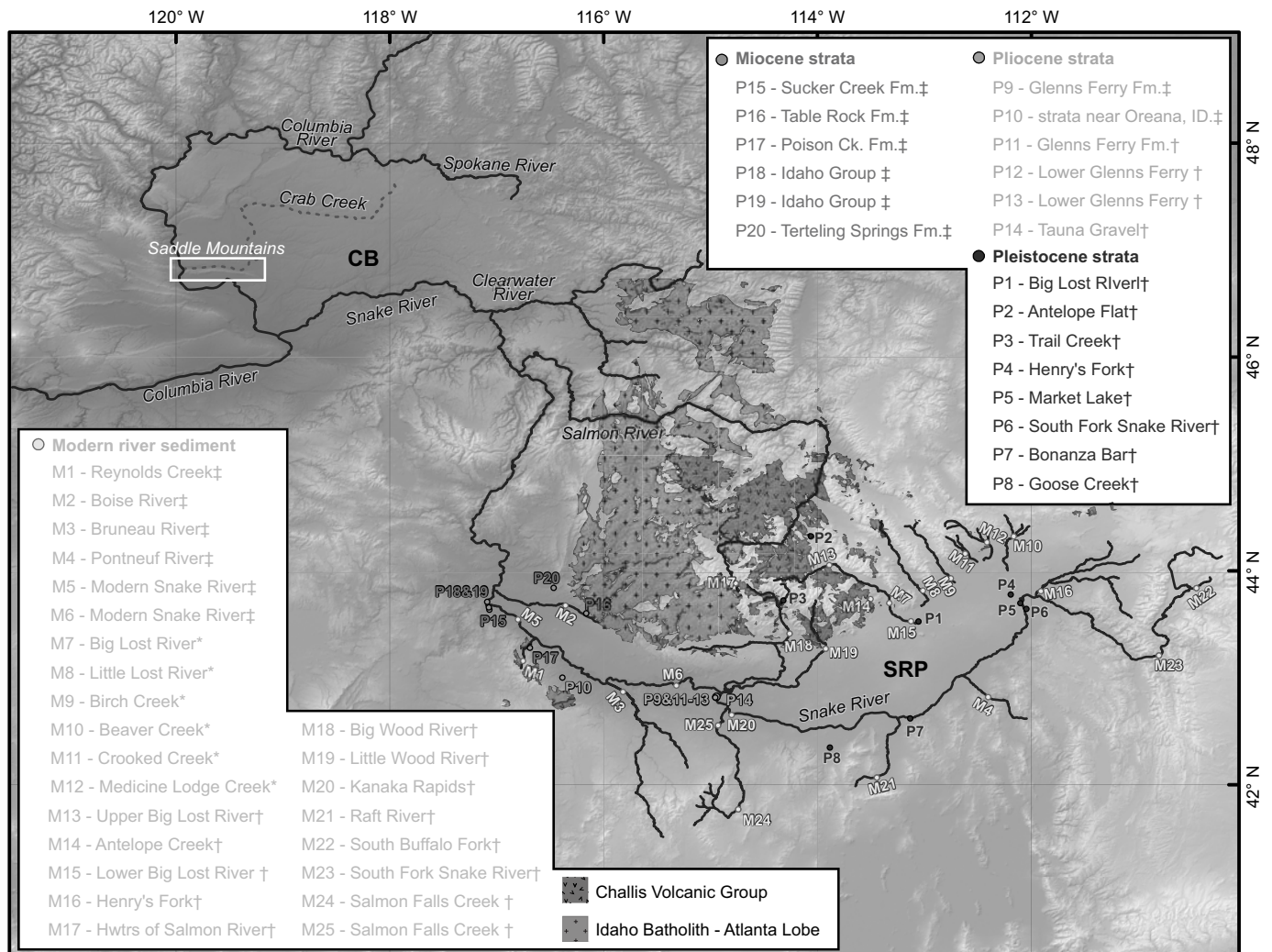








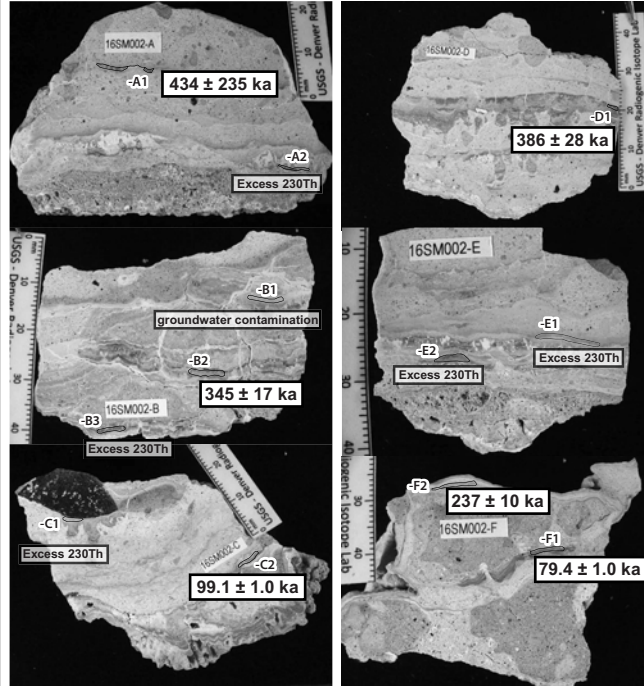




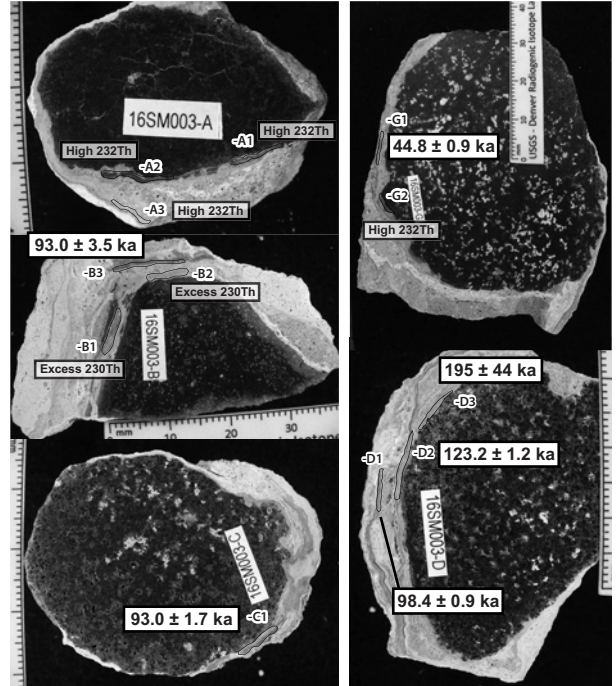
A. 15SM011 - Footwall



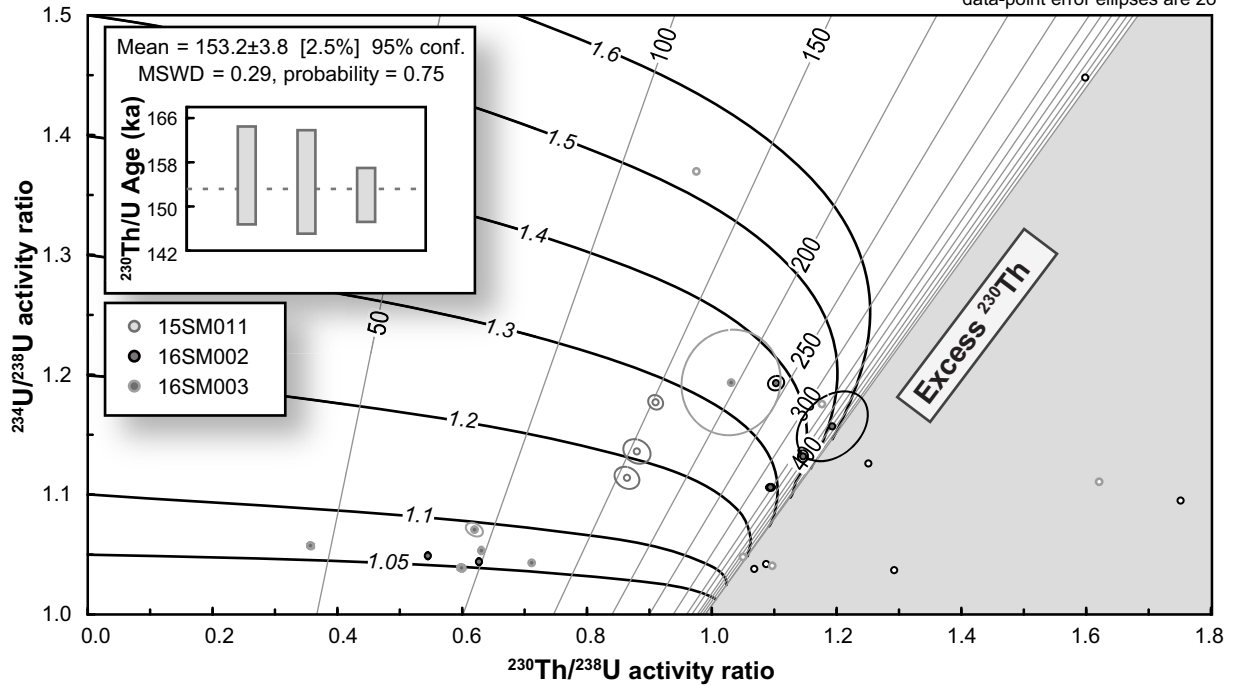
B. 16SM002 - Hanging wall

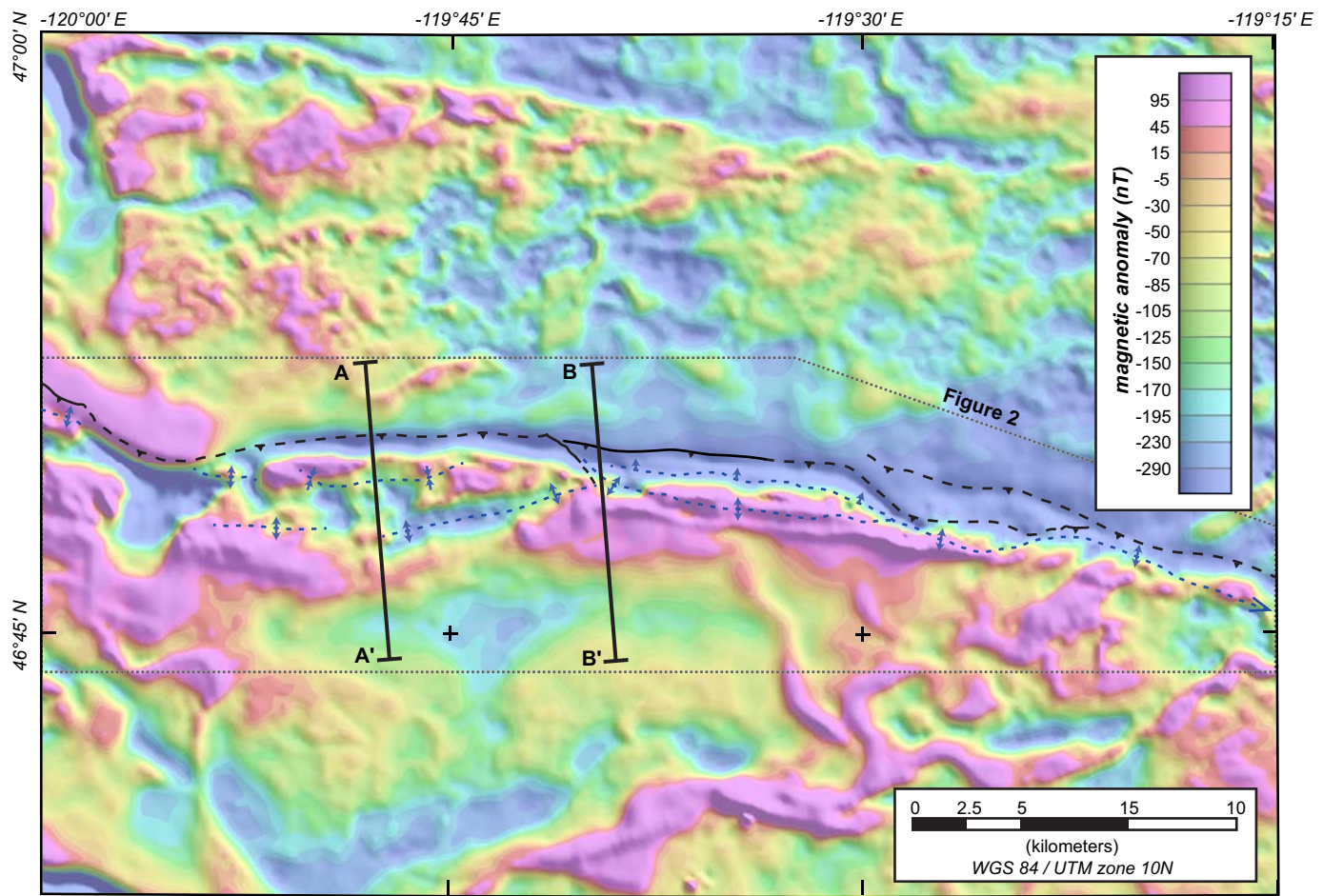


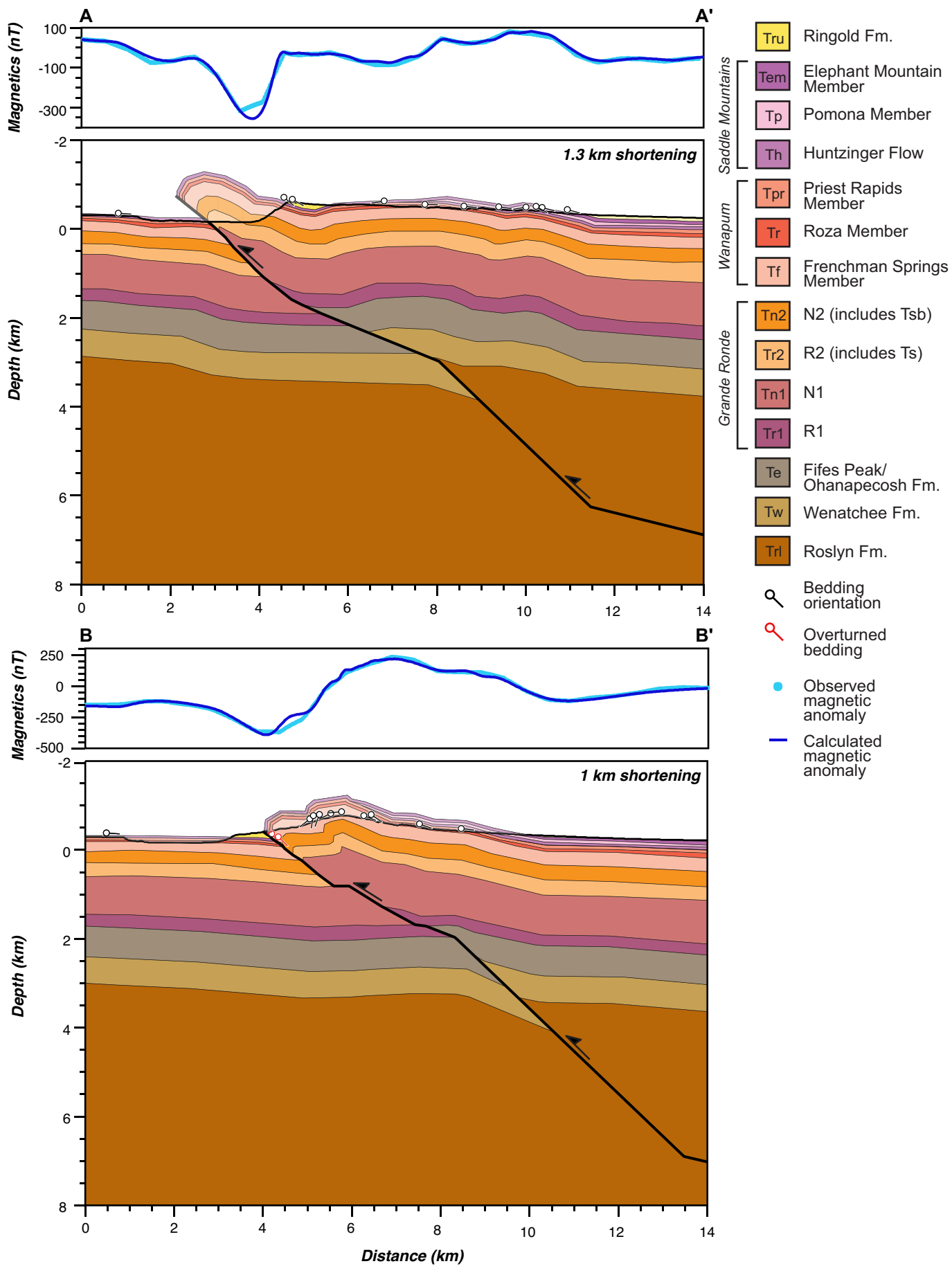
C. 16SM003 - Hanging wall

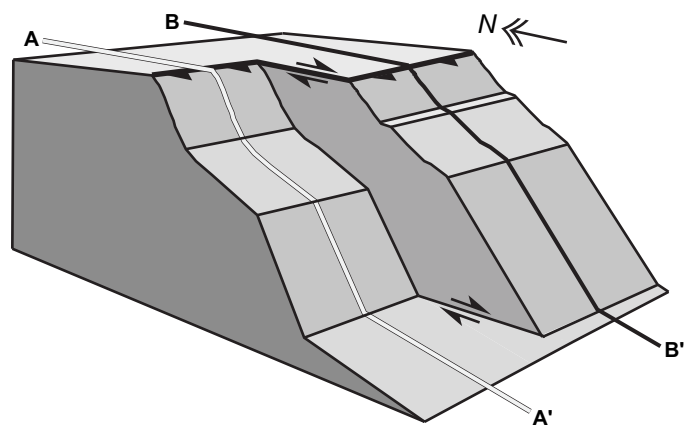
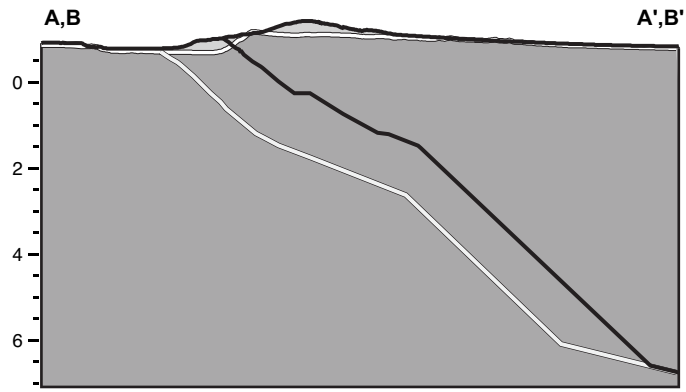


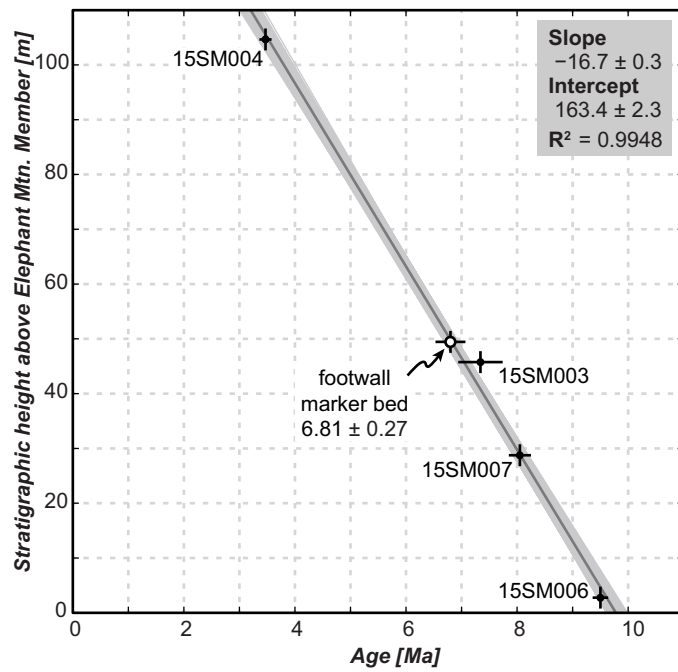
D. Data plot



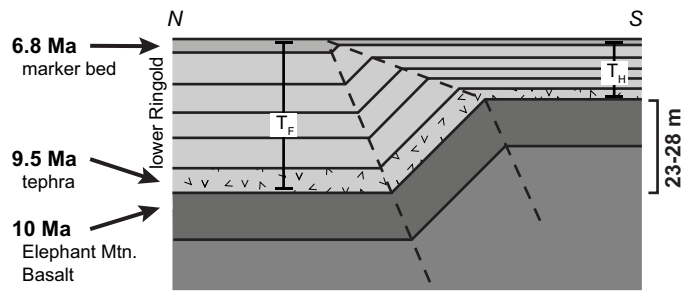




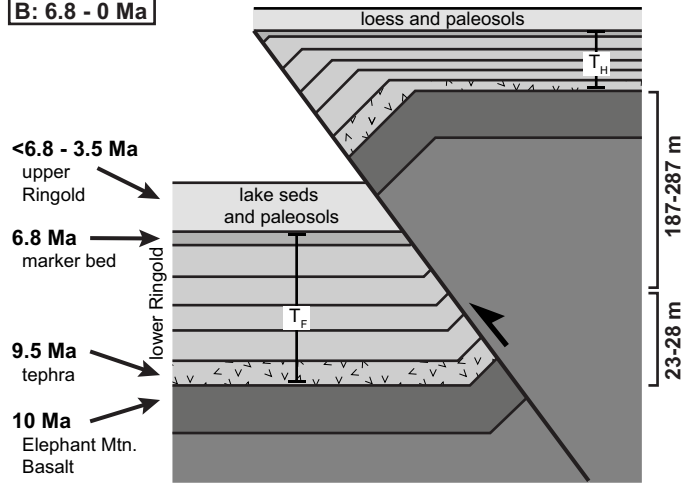




A: 10 - 6.8 Ma



B: 6.8 - 0 Ma



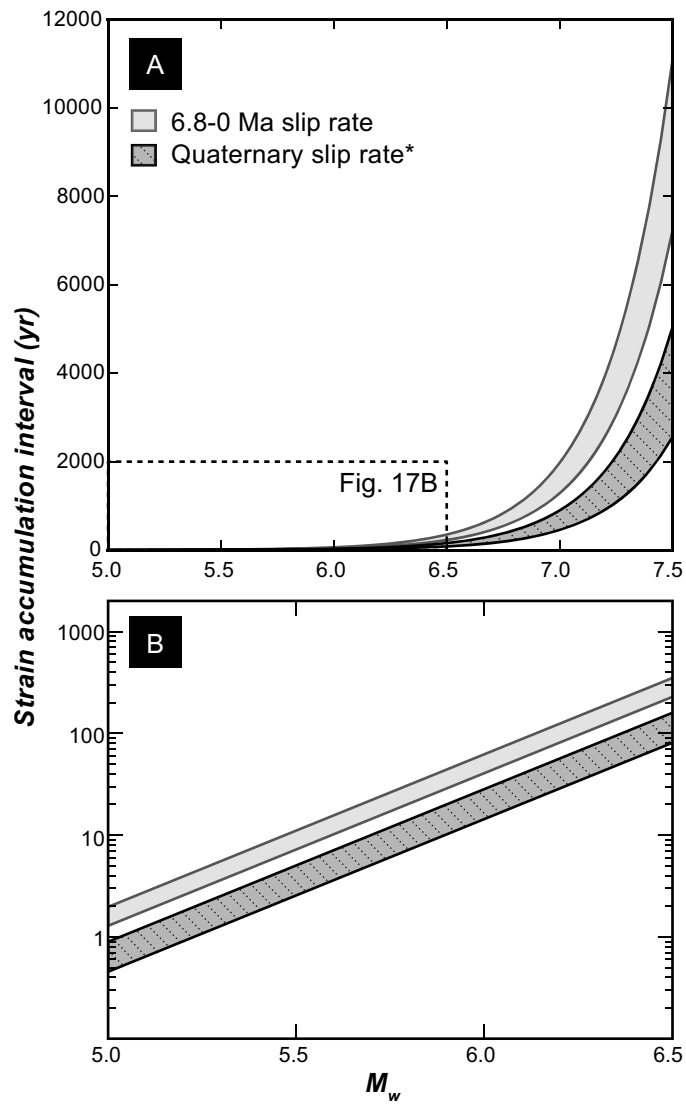


Figure A1. Borehole stratigraphy near the Saddle Mountains anticline, based on original and published interpretations (Wilson et al., 2008; Czajkowski et al., 2012). Original data are downloadable online (www.dnr.wa.gov). The repeated section of CRBG in borehole BN 1-9 is estimated from cross section A-A' and matches with estimates from Reidel et al. (1989a).

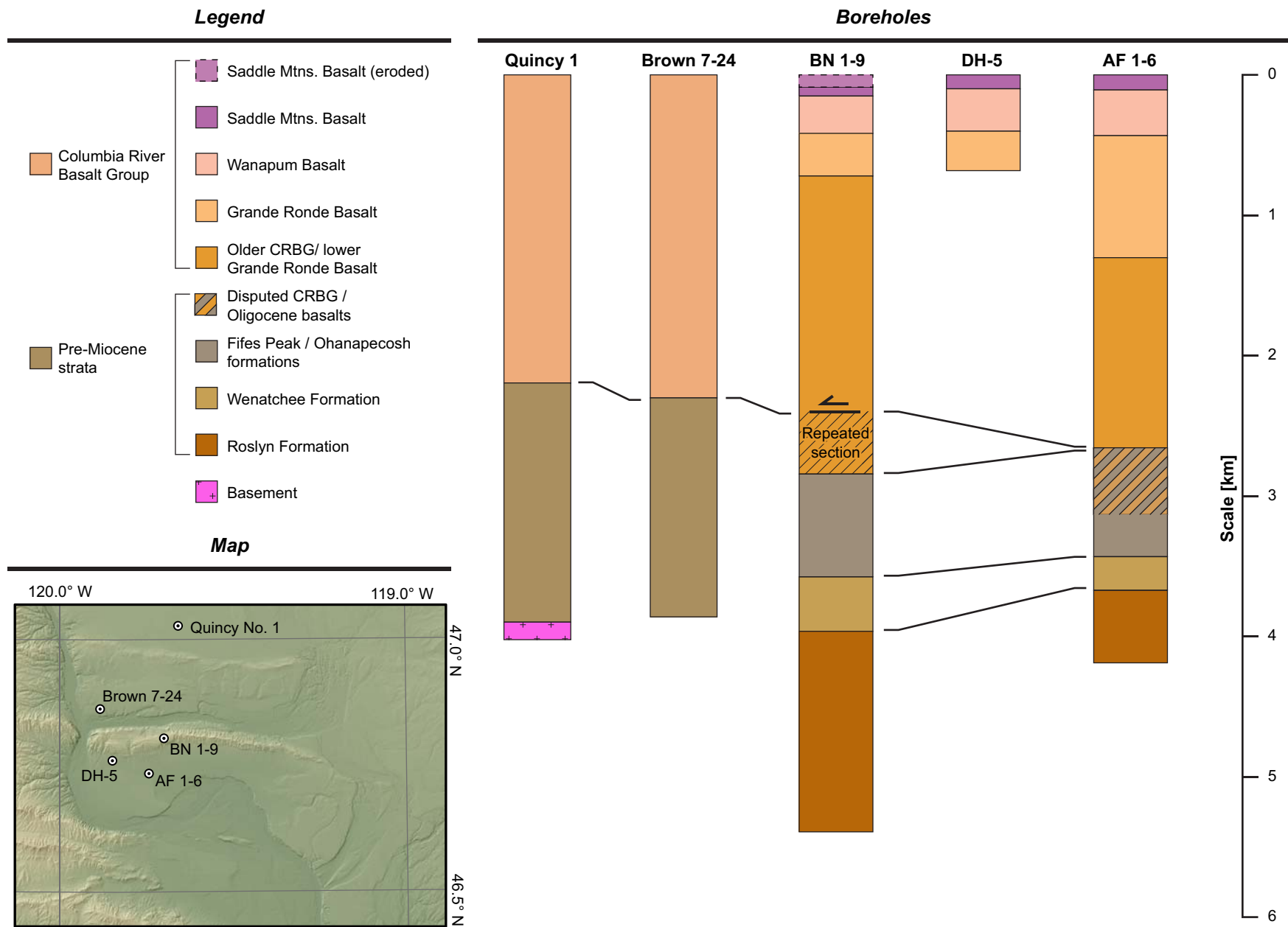


Figure A2. U-Pb ages from 0-250 Ma for the tephra collected from the Ringold Formation near the Saddle Mountains anticline. Samples 15SM002, -007, -006 and 16SM001 show nearly unimodal peaks. This indicates that the zircons are predominantly from the airfall tuff and the youngest age peaks are thus robust measurements of the depositional age. Sample 15SM003 has some more detrital zircon contamination, and the youngest age peak should be regarded as a maximum age of deposition.

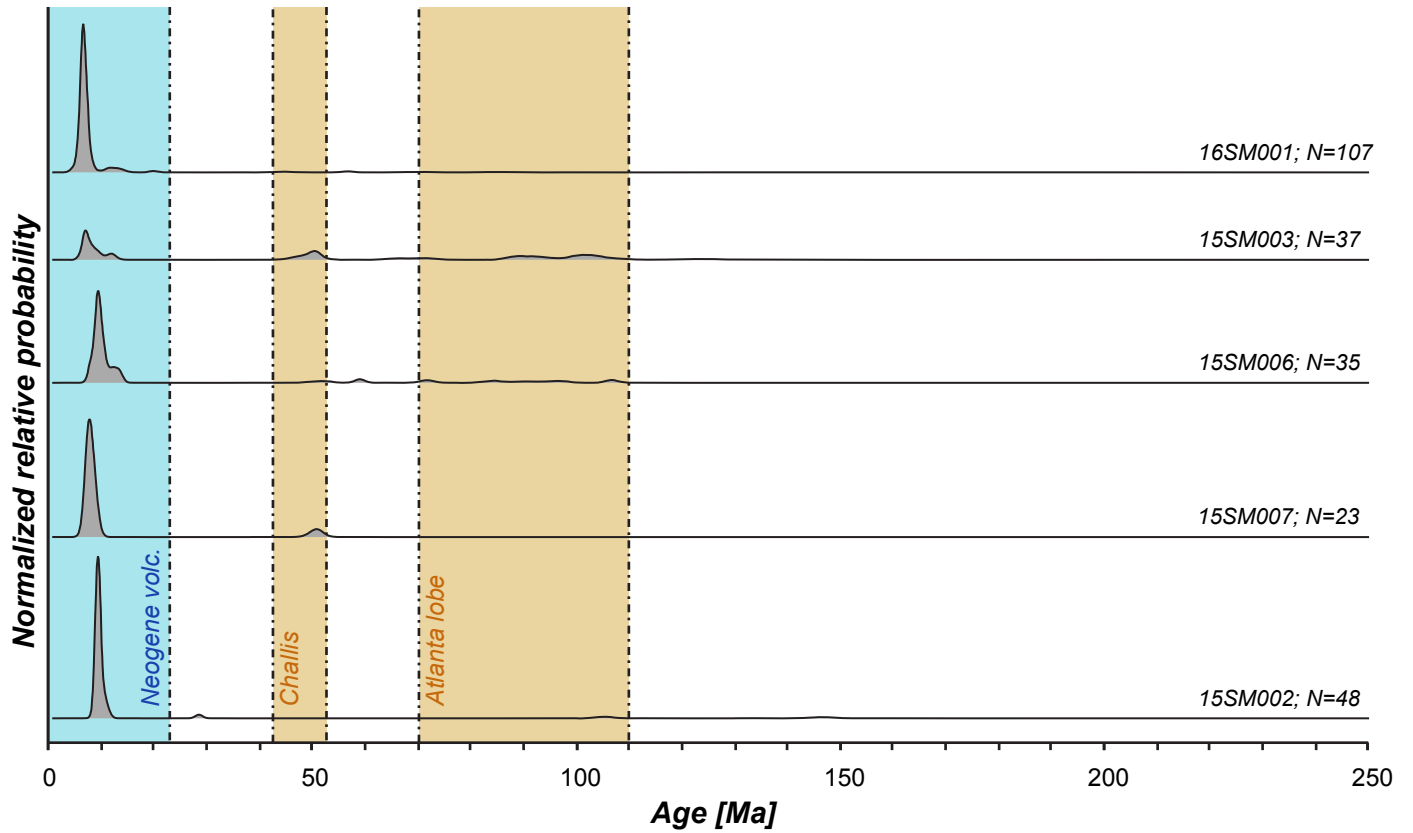


Figure A3. Detrital U-Pb zircon age spectra for the Ringold strata (15SM013, 15SM004) and for the Snake River Plain samples that compare well. Comparison is based in K-S test and Kuiper test p-values and coefficients of overlap, similarity, and cross correlation (Table A9).

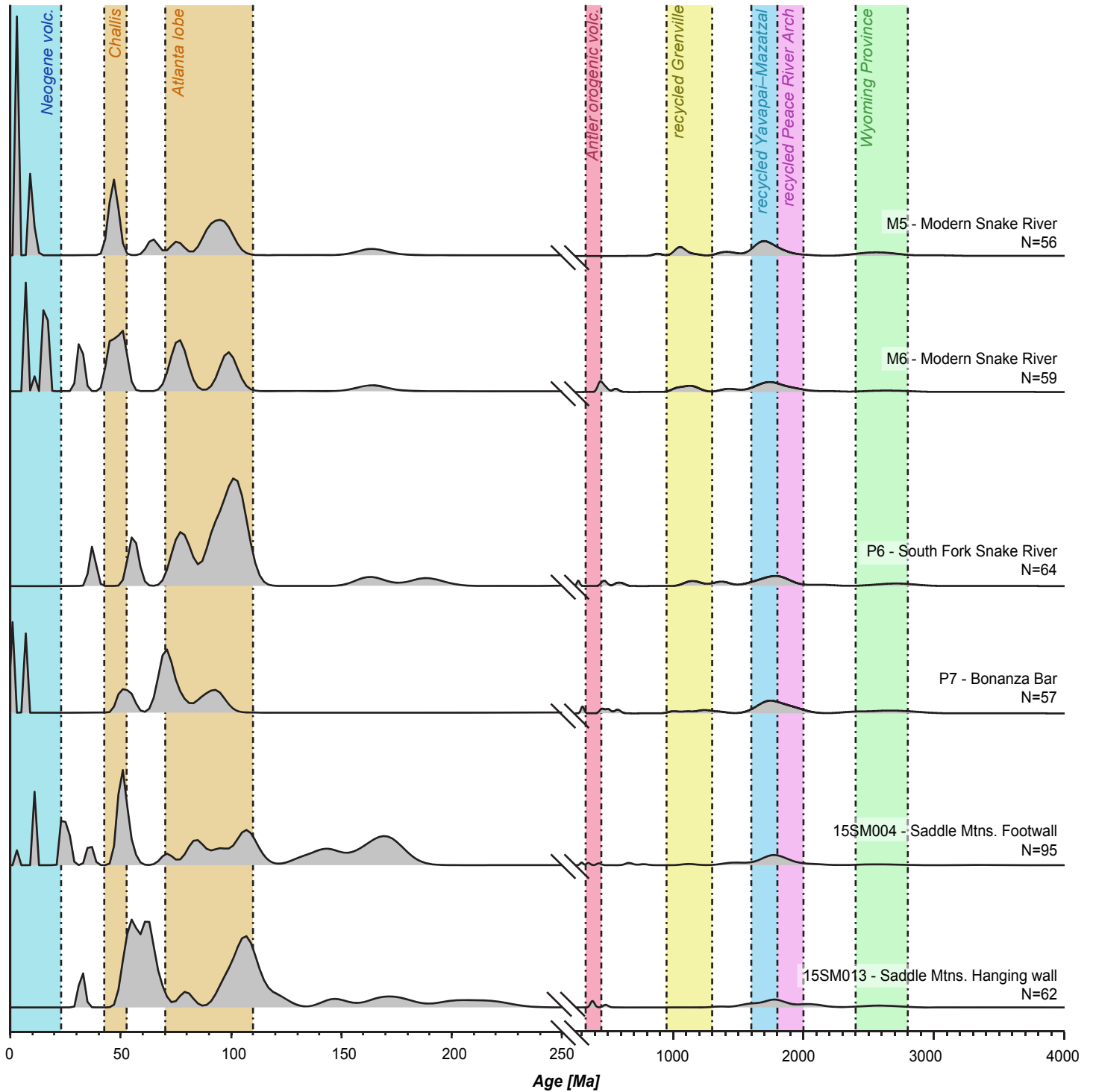


Figure A4. Map of the Saddle Mountains fault and anticline with paleomagnetic data from Reidel et. al. (1984) and Van Alstine and Gillett (1981). Paleomagnetic sample locations are estimated from township and range locations reported in Reidel et al. (1984). Paleomagnetic data are from the Pomoma Member of the Saddle Mountains Basalt (12.0 - 10.9 Ma). Cross section transects A-A' and B-B' are shown for reference. Similar quantities of rotation since 12 Ma are measured near both cross section transects. Greater quantities of rotation to the east occur along the Smyrna Bench and Saddle Gap segments of the Saddle Mountains fault.

